

Integrating Color Features in Polarimetric SAR Image Classification

Stefan Uhlmann, *Student Member, IEEE*, and Serkan Kiranyaz

Abstract—Polarimetric synthetic aperture radar (PolSAR) data are used extensively for terrain classification applying SAR features from various target decompositions and certain textural features. However, one source of information has so far been neglected from PolSAR classification: *Color*. It is a common practice to visualize PolSAR data by color coding methods and thus, it is possible to extract powerful color features from such pseudocolor images so as to provide additional data for a superior terrain classification. In this paper, we first review previous attempts for PolSAR classifications using various feature combinations and then we introduce and perform in-depth investigation of the application of color features over the Pauli color-coded images besides SAR and texture features. We run an extensive set of comparative evaluations using 24 different feature set combinations over three images of the Flevoland- and the San Francisco Bay region from the RADARSAT-2 and the AIRSAR systems operating in C- and L-bands, respectively. We then consider support vector machines and random forests classifier topologies to test and evaluate the role of color features over the classification performance. The classification results show that the additional color features introduce a new level of discrimination and provide noteworthy improvement in classification performance (compared with the traditionally employed PolSAR and texture features) within the application of land use and land cover classification.

Index Terms—Classification, color features, evaluation, feature extraction, polarimetric radar, synthetic aperture radar (SAR).

I. INTRODUCTION

SYNTHETIC aperture radar (SAR) is a remote sensing technique operating in the microwave frequency range, where it provides low- to high-resolution images of an earth surface using the reflected (i.e., backscattered) wave signals received from the observed area. To obtain the final 2-D image, all received signals over a period of time are synthesized using signal processing techniques. Generally, an airborne or spaceborne SAR system operates within the electromagnetic spectrum from P-band (0.3 GHz) up to K_a -band (40 GHz) in a side-looking geometry, where a transmitted wave is perpendicular to the system's flight direction. The benefits of such a system are manifold, the most important properties of which being: 1) backscatter sensitivity to terrain and object characteristics; 2) ability to operate in all-weather conditions (i.e., clouds, fog, rain, smoke, and day/night); 3) coherent

Manuscript received August 8, 2012; revised March 11, 2013; accepted April 3, 2013.

The authors are with the Department of Signal Processing, Tampere University of Technology, Tampere 33720, Finland (e-mail: stefan.uhlmann@tut.fi; serkan@cs.tut.fi).

Color versions of one or more of the figures in this paper are available online at <http://ieeexplore.ieee.org>.

Digital Object Identifier 10.1109/TGRS.2013.2258675

imaging (both amplitude and phase signals) capability; and 4) transmission/reception of polarized radar waves (polarization diversity). Hence, these properties are highly advantageous to optical and spectral remote sensing systems.

Over the last three decades several airborne and spaceborne SAR systems have been developed supporting single-, dual-, and quad-polarizations such as AIRSAR, EMISAR, E-SAR, RAMSES, and SETHI as airborne systems; ENVISAT-ASAR, ALOS-PALSAR, RADARSAT-2, TerraSAR-X, and COSMO-SkyMed as spaceborne systems. More details to several of these systems can be found in [1]. There are still further developments for future spaceborne systems such as the ESA's Sentinel satellites [2].

The field of SAR classification has received a lot of attention in the past years because of the large variety of available data from these airborne and spaceborne radar systems. Especially, land use/land cover (LULC) classification is one of the major applications using quad-pol (fully polarimetric) SAR image data benefiting from the aforementioned SAR properties. As for general classification tasks, there are supervised and unsupervised attempts for SAR classification; the former usually achieve higher classification accuracy. While the main focus in this paper is on supervised classification, we would like to point out that there are recent unsupervised works that incorporate spatial proximity [3] or a spatial context model [4] beside the initial statistical modeling and segmentation to improve clustering and classification. The inclusion of such a spatial model may result in visually smoother and cleaner classification compared with simpler clustering techniques or pixel-based classification approaches on SAR images mainly because of the presence of speckle noise.

The most straightforward approach is to directly apply the polarimetric SAR (PolSAR) data (backscattering coefficients) or the generated covariance/coherency matrix as the underlying features in the LULC classification process. In early approaches, the basic backscattering information of polarimetric data such as HH, HV, and VV channels over single-band data or various combinations over multiband data are used with conventional neural networks (NNs) [5], [6], dynamic learning NN [7], fuzzy NN [8], and maximum likelihood (ML) classifier [9]. Because of the nature of polarimetric data, the covariance matrix provides the complete polarimetric information in amplitude and phase variance as well as correlation for all backscattering elements. Therefore, it is utilized as direct feature input for various classification schemes such as Wishart ML classifier [10]–[12], fuzzy- [13], and complex-valued NN [14].

Over the years, various polarimetric target decompositions (TDs) are developed [15] and we will provide a brief overview on a small selection in Section II. The general idea behind TDs is to describe the average backscattering obtained as the sum of independent components, which provide a better interpretation of the underlying scattering from the measured radar data. These extracted independent components can then be used for information extraction in PolSAR applications. There is still an extensive research in developing new [16], [17] and improved TDs [18] for additional more accurate terrain discrimination. Various single TDs are employed for LULC classification either alone using Bayesian ML [19], NNs [20], and AdaBoost [21], or in combination with the backscattering coefficients applied to AdaBoost [22], random forest (RF) [22], Wishart ML [23], and multimodal Markov aspect model [24]. With more and more TDs available, the investigation of multiple TDs for classification became popular in recent years with and without combination of backscattering information through the application of traditional classifier schemes such as ML [10], NNs [25], [26], support vector machines (SVMs) [26]–[28], and decision tree classifiers [28], [29] or more unconventional classifiers such as object-oriented image classification [30] and conditional random fields [31].

Besides the two aforementioned traditionally used PolSAR features, backscattering elements, and TD components, which are based on the physical, geometrical, and scattering properties of targets, the incorporation of textural information as an image processing method is one of the most popular feature in SAR classification. More than two decades ago, Shanmugan *et al.* [32] evaluated gray-level co-occurrence matrix (GLCM) features [33] for radar images and Ulaby [34] added first- and second-order statistics over SAR intensity images to evaluate and classify Seasat SAR and SIR-A data. After that various evaluation and classification approaches over SAR data using only textural information are reported with GLCM being the dominant method [24], [35]–[41]. In addition, investigations also included fractal features [39], [42], wavelets and semi-variogram [42] as well as recently gabor wavelets [37], [40] and histogram of gradients [40]. In 2011, Dai *et al.* [43] proposed the multilevel local pattern histogram as a novel descriptor of SAR images, which captures local and global structural information while being robust to speckle noise. They demonstrated its performance by outperforming GLCM and gabor wavelets.

Texture, as a single feature, has proven as a valuable resource for SAR classification. Therefore, it is an obvious choice to combine SAR features with textural information to improve classification results. Basic attempts started with simply adding backscattering together with GLCM [24] or wavelets [44], before the covariance or coherency matrix with different TD components are also used with GLCM [36], [41], wavelets [45] as well as gabor wavelets [46], and Markov Random Fields [47]. A recent research combined a large amount of different features (i.e., backscattering elements, GLCM, and components of 13 polarimetric TDs) for LULC classification of RADARSAT-2 data employing an object-oriented approach using a decision tree algorithm [38]. Even though texture is the most common visual feature, there is an on-going investigation

in the direction of polarimetric time-frequency signatures of scatterers for the classification of man-made targets [48] as well as applying bag-of-features and pyramid-representation over single-channel TerraSAR-X data [49].

There are various attempts to tackle PolSAR classification from using little to large feature combinations, whereas texture is playing an extensive role. However, there is one feature that is mostly ignored from PolSAR classification so far: *Color*. For instance, in a recent survey paper [50], covering several techniques for improving classification performance of remote sensing data, no color-based feature is considered. However, for visualization purpose it is a common practice to generate pseudocolor images by mapping backscattering elements or TD components to the different color channels (e.g., the Pauli color coding in the H, V polarization basis). In particular, several approaches have also focused on better color representations of PolSAR images such as assigning same colors to the same scattering information [51], [52], or investigating and comparing different scattering parameters in various color space models for visualization [53]. Turner and Woodhouse [54] have recently undertaken a slightly different yet interesting approach where they did not use image pixels but rather icons (in form of ellipses) to represent the image data hence polarimetric properties and geographic context can be visualized together. Even though these techniques do obviously not provide a natural color representation, color features extracted from pseudocolor images of PolSAR data may provide valuable cues for describing SAR terrain classes.

In this paper, we focus on investigating the potential of the extracted color features for the purpose of superior performance in supervised PolSAR classification and we aim to accomplish this by using various visual color descriptors [55]. Similar to texture features, color features are frequently used in the areas of content-based image retrieval [56] and other computer vision areas [57] such as object recognition and image categorization. In PolSAR applications, texture features are generally extracted over intensity images generated from the different backscattering matrices, e.g., HH, HV, or VV. In this paper, the main objective is to extract powerful color features from a pseudocolor-coded image, in particular, the Pauli color coding in the H, V polarization basis, and to evaluate their discrimination power with several combinations of PolSAR and texture features. To accomplish this, we will provide extensive experiments over three PolSAR images from an airborne (AIRSAR) and a spaceborne (RADARSAT-2) system considering two different band spectra, *C* and *L*, over two well-known classifiers, SVMs and RFs, both of which are becoming more popular in this field.

The rest of this paper is organized as follows. We introduce and describe the major PolSAR and image processing features employed along with their extraction and normalization procedure in Section II. Section III describes the different PolSAR image data and classifiers used within these experiments, and Section IV describes an extensive set of classification results with combinations of PolSAR, texture, and color features over the PolSAR image data and performs comparative evaluations for major classifier schemes. Finally, Section V concludes the paper and discusses topics for future work.

II. PoLSAR IMAGE PROCESSING

The first part of this section describes a wide variety of PoLSAR features used in this paper and discusses how they are formed to feature vectors and therefore they can be combined into sets as inputs for the classifiers. The second part describes the application of image processing approaches such as texture and in particular color features over pseudocolor images generated by color coding schemes using different backscattering components or PoLSAR feature combinations.

A. SAR Feature Extraction and Normalization

When acquiring data from radar systems, the effects of speckle noise and random scattering from the target surface require a multivariate statistical description. Therefore, finding a way of describing average or dominant scattering is beneficial for the task of classification.

PoLSAR features can generally be divided into two categories: 1) belongs to the features extracted directly from the PoLSAR data (backscattering coefficients) and its different transforms such as the scattering matrix, and from which the covariance matrix and the coherency matrix can be derived and 2) is based on the polarimetric TD theorems, which try to describe the obtained average scattering as the sum of independent components and can then be used for information extraction in PoLSAR applications.

Two theories of TD can be distinguished: 1) coherent TD and 2) incoherent TD. Coherent TD theory characterizes completely polarized scattered waves for which the scattering matrix holds the fully polarimetric information. However, generally, the scattered wave is partially polarized and extracting geophysical parameters from a natural target surface with incoherent scatterers is usually of more interest. Hence, the development of the incoherent TD theory is developed to represent a target-averaged matrix into a sum of single-scattering matrices, which provides a better interpretation of the underlying scattering and simpler ways of extracting the geophysical parameters from the measured radar data [15], [58].

PoLSAR systems often measure the complex scattering matrix, $[S]$, produced by a target under study with the objective to infer its physical properties. With linear horizontal (h) and vertical (v) polarizations for transmitting and receiving, $[S]$ can be expressed as follows:

$$[S] = \begin{bmatrix} S_{hh} & S_{hv} \\ S_{vh} & S_{vv} \end{bmatrix} \quad (1)$$

where reciprocity theorem applies in a monostatic system configuration (i.e., for airborne systems) yields $S_{hv} = S_{vh}$.

The coherent TD theorems aim to express the scattering matrix measured by the radar as the combination of scattering responses of coherent scatterers. One way to analyze coherent scatter targets is the Pauli decomposition [15], which expresses $[S]$ as the sum of the Pauli matrices as follows:

$$\begin{aligned} [S] &= \begin{bmatrix} S_{hh} & S_{hv} \\ S_{vh} & S_{vv} \end{bmatrix} = \alpha [S]_a + \beta [S]_b + \gamma [S]_c \text{ where} \\ \alpha &= (S_{hh} + S_{vv}) / \sqrt{2} \\ \beta &= (S_{hh} - S_{vv}) / \sqrt{2} \\ \gamma &= \sqrt{2} S_{hv}. \end{aligned} \quad (2)$$

Hence by means of the Pauli decomposition, all polarimetric information in $[S]$ could be represented by combining the intensities $|\alpha|^2$, $|\beta|^2$, and $|\gamma|^2$ that determine the power of different types of scatterers such as single- or odd-bounce scattering, double- or even-bounce scattering, and orthogonal polarization by volume scattering.

The Krogager decomposition [59], as another coherent TD, exploits that it is possible to uniquely decompose any complex symmetric radar target scattering matrix into the physical interpretation of three components, in this particular case, a sphere, an oriented diplane, and a right or left wound helix. In the linear orthogonal basis (h, v) for the scattering matrix, the Krogager decomposition has the formulation as follows:

$$[S_{(h,v)}] = e^{j\varphi} \left(e^{j\varphi s} k_s [S]_s + k_d [S]_d + k_h [S]_h \right) \quad (3)$$

where k_s , k_d , and k_h are the weights of the sphere, the diplane, and the helix components, respectively. Its main goal is to resolve different scattering characteristics independent from the incidence angle.

Alternatively, the incoherent TDs employ the second-order polarimetric representations of PoLSAR data (such as covariance matrix $\langle [C] \rangle$ or coherency matrix $\langle [T] \rangle$) to characterize distributed scatterers. The second-order polarimetric descriptors of the 3×3 average polarimetric covariance and coherency matrices can be derived from $[S]$ and are employed to extract physical information from the observed scattering process. Because of presence of speckle noise and random vector scattering from surface or volume, PoLSAR data are often multilook processed by averaging n neighboring pixels. By using the Pauli-based scattering vector, \underline{k} , and Lexicographic scattering vector, $\underline{\Omega}$, the multilook coherency matrix $\langle [T] \rangle$, and covariance matrix $\langle [C] \rangle$ can be written as $\langle [T] \rangle = \langle \underline{k} * \underline{k}^T \rangle$ and $\langle [C] \rangle = \langle \underline{\Omega} * \underline{\Omega}^T \rangle$.

Both $\langle [C] \rangle$ and $\langle [T] \rangle$ are 3×3 Hermitian positive semi-definite matrices, and contain the same information regarding the polarimetric scattering amplitudes, phase angles, and correlations. Anyhow, $\langle [T] \rangle$ can be considered to be closer to the physical and geometrical scattering properties, whereas $\langle [C] \rangle$ is directly related to the system measurables [1].

The phenomenological Huynen decomposition [60] represents the first attempt to consider decomposition theorems for the analysis of distributed scatterers. In its parameterization for $\langle [T] \rangle$, it consists of nine independent parameters allowing a physical interpretation of the target under consideration where the three elements A_0 , $B_0 + B$, and $B_0 - B$ representing surface, double-bounce, and volume scattering in distributed targets and otherwise relating to the total scattered power from the regular (smooth and convex) parts of the scatterer, the total symmetric, and nonsymmetric depolarized power, respectively, for pure targets.

Based on $\langle [T] \rangle$, the Cloude–Pottier decomposition [15] applies eigenanalysis such as follows:

$$\langle [T] \rangle = \lambda_1 e_1 e_1^* + \lambda_2 e_2 e_2^* + \lambda_3 e_3 e_3^* \quad (4)$$

where $\lambda_1 > \lambda_2 > \lambda_3 \geq 0$ are real eigenvalues and the corresponding orthonormal eigenvectors e_i (representing three scattering mechanisms). Further, Cloude and Pottier defined

entropy H , a set of four angle averages $\bar{\alpha}, \bar{\beta}, \bar{\delta}$, and $\bar{\gamma}$, and anisotropy A for the analysis of the physical information related to the scattering characteristics of a medium based on the eigenvectors and eigenvalues. For a multilook coherency matrix, the entropy, $0 \leq H \leq 1$ is the randomness of a scattering medium between isotropic scattering ($H = 0$) and fully random scattering ($H = 1$), while the average angle $\bar{\alpha}$ can be related to the target average scattering mechanisms from a single-bounce (or surface) scattering ($\bar{\alpha} \approx 0$), dipole (or volume) scattering ($\bar{\alpha} \approx \pi/4$), and double-bounce scattering ($\bar{\alpha} \approx \pi/2$). Because of the basis invariance of the TD, H and $\bar{\alpha}$ are roll invariant, hence they do not depend on the orientation of the target in the radar line of sight. In addition, information about a target's total backscattered power can be determined by the so-called Span, which is defined as the sum over the three largest eigenvalues. Entropy H , estimate of the average angle $\bar{\alpha}$, and the Span are commonly used as polarimetric features of a scatterer in many target classification schemes [19], [23], [25]–[28], [31], [36], [38], [41], [47].

The Touzi decomposition [61] similar to the Cloude-Pottier's decomposition, is also, based on the incoherent characteristic decomposition of $\langle[T]\rangle$. For a reciprocal target, it permits the representation of $\langle[T]\rangle$ as the incoherent sum of up to three coherency matrices $[T]_i$ representing three different single scatterers, each weighted by its appropriate positive real eigenvalue λ_i . Compared with the Cloude-Pottier decomposition, Touzi's decomposition differentiates in using a roll invariant coherent scattering model for the parameterization of the coherency eigenvectors in terms of their unique target characteristics. For noninterferometric applications, the absolute target phase Φ_s can be ignored, and the coherent scatterer is uniquely characterized with five independent parameters, such as, $\alpha_s, \phi_{\alpha_s}, \psi, \tau_m$, and m with α_s and ϕ_{α_s} being the polar coordinates of the symmetric scattering type; ψ, τ_m , and m are Huynen's orientation angle, helicity, and maximum amplitude parameters.

Van Zyl first considered eigenvector/eigenvalue analysis of $\langle[C]\rangle$ to describe symmetrical natural terrain in the monostatic case [58] as follows:

$$\langle[C]\rangle = \sum_{i=1}^3 \lambda_i \underline{u}_i \cdot \underline{u}_i^{*T} = [C]_s + [C]_d + [C]_v \quad (5)$$

where λ and \underline{u} are eigenvalues and eigenvectors, respectively. This expression represents a three components scattering model where the first two eigenvectors represent equivalent scattering matrices that can be interpreted with single- and double-bounce scatterings, and the third one corresponds to volume scattering. In addition, based on this eigenvalue analysis, Kim and van Zyl [62] introduced an estimation of (forest) biomass from PolSAR data, the so-called radar vegetation index (RVI) (also generally characterized in [63]) defined as follows:

$$RVI = \frac{4 \min(\lambda_1, \lambda_2, \lambda_3)}{\lambda_1 + \lambda_2 + \lambda_3} \left(= \frac{8\sigma_{hv}}{\sigma_{hh} + \sigma_{vv} + 2\sigma_{hv}} \right) \quad (6)$$

where the sigma's are the cross- and co-polarization radar scattering cross sections. The representation by the eigenvalues is the general characterization of the RVI whereas in the

brackets is the alternative but more restrictive definition [62] that is only valid for a medium with reflection symmetry and can be expressed as $RVI = 4\lambda \cdot 2$ [63].

Van Zyl's decomposition of $\langle[C]\rangle$ is also considered to be the starting point for the so-called model-based decompositions such as Freeman [64] and Yamaguchi [65] decompositions. The Freeman decomposition describes the covariance matrix, $\langle[C]\rangle$, as a combination of three simple scattering mechanisms, such as volume scatter from a cloud of randomly oriented dipoles, even-bounce (double-bounce) scatter from a pair of orthogonal surfaces with different dielectric constants, and Bragg (single-bounce) scatter from a moderately rough surface. The Freeman decomposition follows the same expression for $\langle[C]\rangle$ as van Zyl, see (5). The scattering powers for single-bounce, P_s , double-bounce, P_d , and volume scattering, P_v , are estimated as follows:

$$P_s = f_s (1 + |\beta|^2), \quad P_d = f_d (1 + |\alpha|^2) \quad \text{and} \quad P_v = \frac{8f_v}{3} \quad (7)$$

where f_s , f_d , and f_v are the contribution of single-bounce, double-bounce, and volume scattering of $\langle[C]\rangle$, α and β are the surface and double-bounce scatter, respectively. This composite scattering model is generally used to discriminate the polarimetric backscatter of different natural surface cover types from naturally occurring scatterers' particularly forest-like vegetation.

Yamaguchi *et al.* [65] introduced a four-component scattering model based on $\langle[C]\rangle$ (single- and double-bounce, volume, and helix scattering power contributions) that extends the three-component decomposition method introduced by Freeman. The helix scattering term is added to address the co- and the cross-pol correlations that generally appear in complicated geometric scattering structures and is nonexistent for natural distributed scatterer. Hence, this term is mainly relevant for describing man-made targets in urban areas. The scattering powers for P_s and P_d are equivalent to Freemans', i.e., (7), whereas P_c is defined and P_v is modified according to the following:

$$P_c = 2 |\text{Im} \langle S_{hv}^* (S_{hh} - S_{vv}) \rangle|, \quad P_v = \frac{15}{2} \left(\langle |S_{hv}|^2 \rangle - \frac{f_c}{4} \right) \quad (8)$$

with Im being the imaginary part of a complex matrix. However, there is the issue, as for all model-based decompositions, in overestimating the volume scattering caused by a large cross-polarization component. To overcome this problem, a rotation method of the coherency matrix is proposed by Yamaguchi *et al.* [66]. Anyhow, the discrimination of vegetation and oriented buildings within the same volume scattering is a still existing problem, which is improved by an extended volume scattering model [18].

As a result of the previously reviewed TDs, we form the following five PolSAR feature vectors (FV_N), which will be used to generate the PolSAR feature sets (FSs) applied in these experiments in Section IV. Each FV has the following components selected from the aforementioned PolSAR TD features:

Elements from $\langle [T] \rangle$ and $\langle [C] \rangle$

$$\text{FV}_1 = [T_{11}, T_{22}, T_{33}, C_{12}, |C_{12}|, \angle C_{12}, C_{13}, |C_{13}|, \angle C_{13}, C_{22}, |C_{23}|, \angle C_{23}, C_{33}]. \quad (9)$$

Components of $H/\alpha/A$. and eigenvalue decomposition

$$\text{FV}_2 = [\text{span}, H, A, \bar{\alpha}, \bar{\beta}, \bar{\delta}, \bar{\gamma}, \lambda_1, \lambda_2, \lambda_3, \text{RVI}]. \quad (10)$$

Components from Pauli, Krogager, and Touzi decomposition

$$\text{FV}_3 = [|\alpha|^2, |\beta|^2, |\gamma|^2, k_s, k_d, k_v, \alpha_s, \Phi_{\alpha_s}, \psi, \tau_m]. \quad (11)$$

Components from Freeman and Huynen

$$\text{FV}_4 = [P_s, P_d, P_v, 2\langle A_0 \rangle, \langle B_0 \rangle + \langle B \rangle, \langle B_0 \rangle - \langle B \rangle]. \quad (12)$$

Components from VanZyl and Yamaguchi

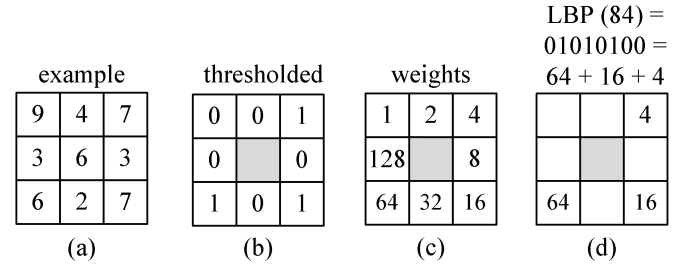
$$\text{FV}_5 = [\lambda_1, \lambda_2, \lambda_3, P_s, P_d, P_v, P_c]. \quad (13)$$

For the normalization purpose, all extracted PolSAR features in FV_1 – FV_5 are linearly scaled to $[-1, 1]$.

We consider the elements from $\langle [T] \rangle$ and $\langle [C] \rangle$ as they are basic representations of the PolSAR data directly derived from the scattering matrix, $[S]$. The Huynen decomposition is selected as it is the first approach to decompose $\langle [T] \rangle$ into independent components. Similarly, the components of $H/\alpha/A$ and the eigenvalue decomposition are chosen as this is considered the first eigenvector-based decomposition and one of the most commonly used TD in PolSAR classification. As derived from the eigenvalues, RVI is considered as an additional discrimination for *vegetation*. Regarding other TD components, some of them extend the existing methods by considering different coherent scatterings (Touzi), different physical interpretations of the underlying scattering (Pauli and Krogager), or they are designed to discriminate particular terrain classes such as *vegetation* (VanZyl and Freeman) or man-made areas (Yamaguchi).

B. Extraction of Visual Features

Besides the application of PolSAR features as described in previous section, the integration of visual features in form of texture is widely applied to extend the feature set within the field of SAR image classification. Generally, PolSAR features provide a description purely on pixel-based level, which will limit discrimination for similar terrain classes because of variations in these terrain surfaces such as different forest types or man-made areas. By employing texture features, the underlying spatial variability of a particular terrain class can be better exploited. Earlier analysis of texture as a feature in SAR classification concluded that texture may, in fact, be more useful than image tone in interpreting radar images [34]. Even though this is related to simple image intensities the general assumption is still valid. Therefore, exploiting pixel relations in close vicinity in the form of texture features (e.g., GLCM) is highly valuable and contributes a major discrimination capability [32]. Along with texture, we will also extract and integrate several color features to further augment our feature sets to improve class discrimination and classification accuracy. These features are mainly defined as a part



Rotation invariant version:

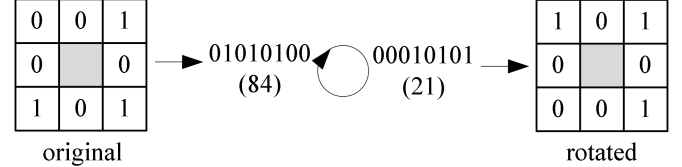


Fig. 1. Computation of rotation invariant LBP value using 3×3 neighborhood.

of the MPEG-7 standard [67] formally called as multimedia content description interface. Its main idea behind the MPEG-7 is to represent information about the multimedia content (e.g., image, audio, and video), but not the content itself (i.e., bits about bits). We will describe the texture and color features employed and show how they are extracted at the end.

1) *Texture Features*: In the field of content-based image retrieval [56], various low-level features are developed to characterize the texture information of an image or image region. So far among popular texture features such as local binary pattern (LBP) [68], the edge histogram descriptor (EHD) [55], gabor wavelets [69], and the GLCM [33] is the most common texture feature employed in SAR classification [24], [35]–[41].

LBP is a rotation invariant texture feature extracted over an n -by- n pixel neighborhood. It works directly on pixels and their neighborhood as shown in Fig. 1(a). The neighboring pixels are then thresholded by the current center pixel obtaining a texture pattern, as shown in Fig. 1(b) and binomial factors Fig. 1(c) are multiplied by the neighboring positions greater than or equal to the center pixel as in Fig. 1(d). Finally, the sum of the binomial factors yields the LBP value being assigned to the center pixel. This procedure is applied to every pixel in the image, which results in a 256-bin histogram. To obtain a more compact rotation invariant representation, LBP values can be combined as they represent the same texture pattern but in a rotated fashion. This can be achieved by circularly shifting the original texture pattern until its minimum decimal value is attained, shown in the bottom of Fig. 1. This rotated LBP value is used rather than the original. One of the advantages of LBP is its simple design that still provides a powerful texture descriptor.

The EHD is an edge-based texture feature from the family of MPEG-7 descriptors. EHD represents the spatial distribution of five types of edges: four directional edges and one nondirectional edge. In its original form, a given image is first divided into subimages, and local edge histograms for each of these subimages are computed. Edges are roughly grouped into five categories: vertical, horizontal, 45° diagonal,

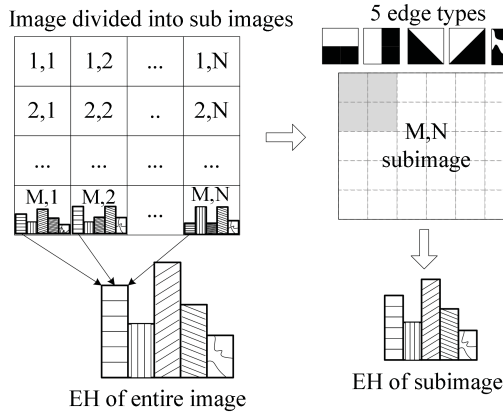


Fig. 2. Accumulation of the edge histogram.

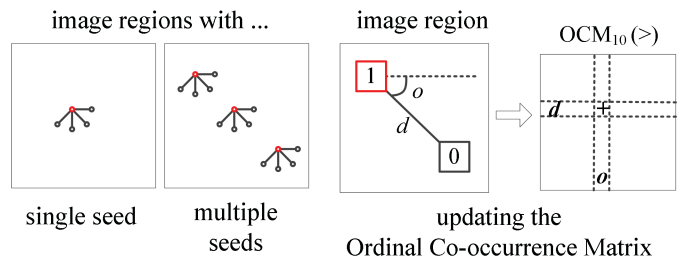
135° diagonal, and isotropic (random) applying simple edge detectors over 2-by-2 image pixel blocks within each subimage. Those image blocks whose edge strengths exceed a certain minimum threshold are used in computing the histogram. Thus, each local histogram has five bins corresponding to the aforementioned five categories. The local histograms from the subimages are combined to generate the five-bin edge histogram representation of the entire image. The procedure for extracting the EHD is shown in Fig. 2.

The popular and powerful signal processing texture descriptor called gabor filter presents a multiresolution approach and was previously applied to SAR classification [37], [40], [46]. The main idea is to process an image region by a bank of filters at different scales and orientations (multichannel) where filtering can be applied in either spatial or frequency domain. An image region $I(x, y)$ that is filtered with a gabor filter g_{mn} results in its gabor wavelet transform W_{mn} , which captures different frequency and orientation information about an underlying texture [69]. W_{mn} can be formulated as follows:

$$W_{mn}(x, y) = \int I(x_1, y_1) g_{mn}^*(x - x_1, y - y_1) dx_1 dy_1. \quad (14)$$

For each scale and orientation, the magnitude response $|W_{mn}|$ is calculated as an output from which the first- and second-order moments are computed as the texture features. Thus, the feature vector is rather small and is formed per scale and orientation.

The ordinal co-occurrence matrix (OCM) [70] approach is a combination of the traditional GLCM and ordinal descriptors (ordinal methods for texture description). Remember that a GLCM entry corresponds to the number of occurrences of a pair of gray levels i and j separated by a displacement $d = (dx, dy)$. Thus, an GLCM entry, $M(i, j)$, is given as, $M(i, j) = |\{(r, s), (t, v): I(r, s) = i, I(t, v) = j\}|$ where $(r, s), (t, v) \in N \times N$, $(t, v) = (r \pm dx, s \pm dy)$, and $|\cdot|$ is the cardinality of a seta set. The similarity between two GLCMs is usually estimated by various properties extracted from them [33]. However, one difference of OCM compared with GLCM is the application of ordinal relationship between the pixels rather than just gray level values. Another alternation is that instead of using just one seed pixel to calculate the displacements, multiple seed pixels are used as shown in the

Fig. 3. OCM with different seed setup to calculate displacements of four orientations from red seed (left) and example of accumulating and updating the relationship matrix OCM₁₀ when the seed pixels is greater than the displacement pixel for distance d and orientation o (right).

left side of Fig. 3, which are able to capture more details within a given image region. This will obviously come with an increase in computational complexity. The constructed features represent the occurrence frequency of certain ordinal relationships such as greater, equal, and smaller at different distances d and orientations o over all the used seed points within a particular image region with an example shown in Fig. 3 (right-hand side). The comparison between two different OCMs can then be done directly by summing the differences of the corresponding distance and orientation relationship matrices. Even though, OCM is not applied as much as GLCM to SAR images, it is anticipated that OCM will perform on a similar level or even better. It is shown that OCM outperforms GLCM in texture classification [70] particularly for coarse textures and irregular pattern as found in man-made areas whereas they both achieve similar results for fine textures and highly repetitive structured pattern as in *water*, *forest* or other *vegetation*.

2) Color Features: Contrary to texture, color features are usually not considered within the classification of PolSAR images as the original PolSAR data do not indeed provide a (natural) color image representation. Yet for visualization purposes it is common practice to create so-called pseudo or false color images by assigning backscatter matrices to the red, green, and blue image component, respectively. Even though they do obviously not provide a natural color representation, they may provide useful information for discrimination in terrain classification besides visualization. Similar to the texture feature extraction, we extract three color features over a pseudocolor image representation from the Pauli color coding in H, V polarization basis: hue-saturation-value (HSV) color histogram [71], MPEG-7 dominant color descriptor (DCD) [55], and MPEG-7 color structure descriptor (CSD) [55].

Color histogram is one of the most basic and widely known features in image processing. Albeit its simplicity, it is powerful in describing major differences and it has been applied over intensity channels of HH, HV, and VV in SAR classification application. Generally, a histogram is a representation of the intensity distribution within an image region usually extracted over each color space component separately. Because of its large amount of information, the different color components are normally quantized to reduce the amount of color levels from millions to thousands or even to just hundreds and perhaps less, so as to make the descriptor representation more compact. We employ the HSV color space [55] because of its

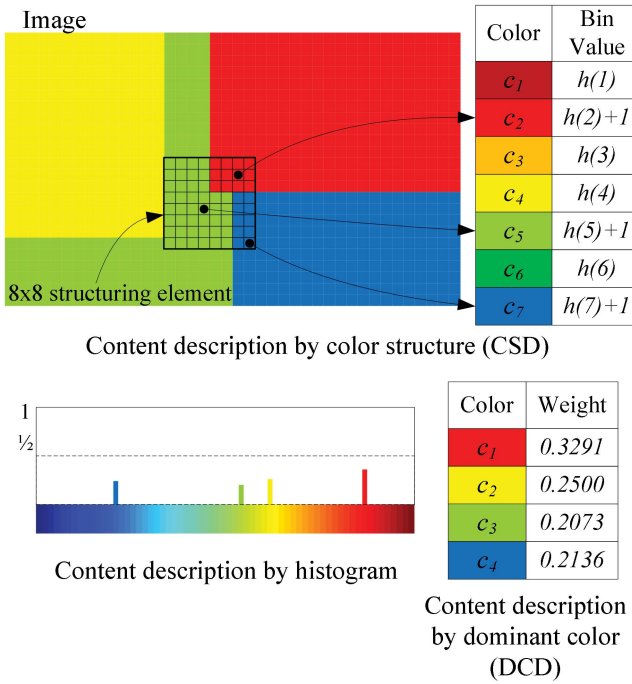


Fig. 4. Accumulation of the color structure histogram (top) and accumulation of the color histogram and DCD (bottom).

component partitioning and its similarity to the human visual system.

The MPEG-7 DCD extracts the most representative colors of a particular color space within an image region where colors are dynamically clustered (i.e., by color distortion and area until a certain number of clusters are obtained). In addition, it is consistent with the human visual system as it mainly perceives prominent colors and discards the rest. Because of this fact, it is possible to sufficiently represent the color content of an image region by a few dominant colors. Bottom of Fig. 4 shows the content description for the histogram and dominant color representation a simple four-color image.

So far, the first two-color features only represent the color distributions of the underlying image region. To further consider the possible relationships among colors, we also extract the MPEG-7 CSD, where its general idea is to describe the local structure in an image region using a sliding 8-by-8 structure element. CSD can be denoted by a histogram where each bin represents the number of structuring elements in the image region containing one or more pixels with a particular color. The operation is shown in the top of Fig. 4, where in its current position three colors are present in the structuring element and the CSD histogram is updated accordingly. Commonly, the image region is first transformed and quantized into the hue-min-max-difference color space [55] to reduce the number of colors before the structuring element is applied.

3) *Composition of Color Feature Vectors:* For visualization of fully polarimetric data, pseudo or false color images can be obtained using H, V polarization basis and assign the backscattering matrices HH, VH, and VV directly to the red, green, and blue image components. Another approach uses \$|HH+VV|\$, \$|HV|\$, and \$|HH-VV|\$ scatter matrices assigned

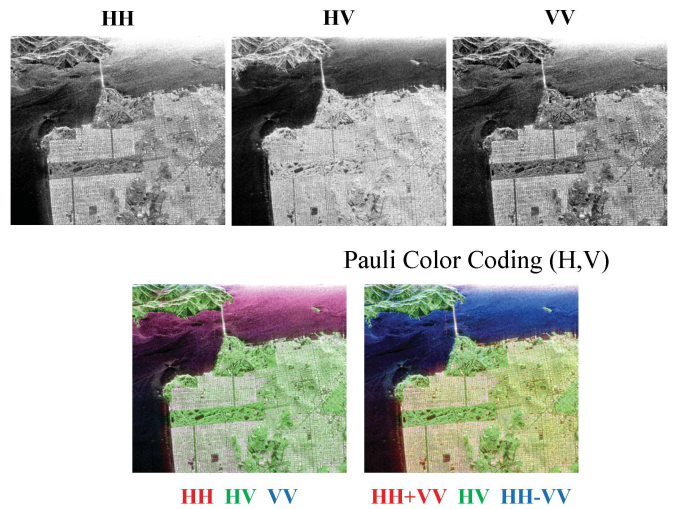


Fig. 5. Visualization of pseudocolor coding in the H, V polarization basis.

to the red, green, and blue image components, and this mapping produces more human-preferable natural colors. This is commonly referred to as Pauli coding representation [72] or Pauli color coding (H, V). Examples for both color coding approaches are shown in Fig. 5. Even though they obviously do not provide a (color) representation as optical remote sensing systems, these pseudocolor images are crucial for visualization, human understanding, and interpretation.

Generally, individual PoLSAR features are pixel-based having a single value per pixel, whereas texture and color features extract statistics over image regions for description. To obtain a description per pixel, we use the surrounding pixel neighborhood to define a small image region. The feature extraction is performed for every pixel over its \$(2w + 1)\$ by \$(2w + 1)\$ pixel neighborhood with \$w = 5\$ as a default setting to keep the pixel neighborhood as compact as possible.

Therefore, we obtain the following seven feature vectors (i.e., four for texture and three for color). Each FVN has the following components selected from the aforementioned features

$$FV_6 = \text{quantized 16 bin LBP histogram} \quad (15)$$

$$FV_7 = 5 \text{ bin MPEG-7 EHD} \quad (16)$$

$$FV_8 = \text{first and second order moments over three scales and four orientation of gabor wavelets} \quad (17)$$

$$FV_9 = \text{three OCM with three distances and four orientations} \quad (18)$$

$$FV_{10} = 24 (6 \times 2 \times 2) \text{ bin HSV histogram} \quad (19)$$

$$FV_{11} = \text{the three color components and the weight of the most dominant color} \quad (20)$$

$$FV_{12} = 32 \text{ bin CSD histogram.} \quad (21)$$

In harmony with the PoLSAR features, all FVs (\$FV_6 - FV_{12}\$) are linearly scaled into \$[-1, 1]\$; hence in total, we extract 141 different image processing features, a total of 81 textural features and 60 color features, respectively.

TABLE I
CLASSIFIERS EMPLOYED WITHIN THE EXPERIMENTAL SETUP

Abbreviation	Description
OvA_RF	One-versus-All using RF
OvA_SVM	One-versus-All using SVM
OvO_RF	One-versus-One using RF
OvO_SVM	One-versus-One using SVM

III. EXPERIMENTAL SETUP

This section describes the setup for the classifiers, PolSAR images, and feature combinations used for all experiments described in Section IV.

A. Classifiers

In the past, various machine learning approaches are utilized for SAR classification. During the last two decades, one of the most commonly used approaches is the ML Classifier and its variants, e.g., [9]–[12], [19], [23], [34], [39], and [47]. However, recently, the focus is drawn to the applications of SVMs [73] and Random Forests (RF) [74] and its variations.

SVM is one of the most commonly used classifier in SAR classification [27], [28], [40], [43], and [46]. As SVM is a binary classifier by nature, there are two main topology approaches to adapt it to multiclass classification: pairwise classification [75], also known as the one-versus-one (OvO) approach, and the one-versus-all (OvA) method [76]. Further, tree classifiers including RF are also frequently applied to SAR classification problems as in [22], [28], [29], [40], and [44]. Similar to the SVM, RF is also a binary classifier, which makes it necessary to use either an OvO or OvA topology, to perform a multiclass classification.

Within these experiments, we aim to cover different classifiers; thus, we focus mainly on SVM and RF because of their recent popularity considering the two topologies, OvO and OvA. Since each topology has its advantages and shortcomings, we shall consider both for individual classification performance analysis. Therefore, Table I shows the four classifier combinations used within our experiments. To determine the best classifier configuration (i.e., kernel and kernel parameters), a sequential search over a range of configurations is performed during the training stage and the best configuration found will be used for PolSAR classification and performance evaluation.

For the SVM implementation, we employ the libSVM library [77] and to find out the best SVM configuration (kernel and kernel parameters), an exhaustive search is conducted for the best kernel type among the linear (LIN), polynomial (POL), radial basis function (RBF), and sigmoid kernel (SIG) along with their individual parameters, i.e., the respectable penalty parameter, $C (2^n; n = 0, \dots, 3)$ and parameter $\gamma (2^{-n}; n = 0, \dots, 3)$ if applicable to the kernel type (e.g., for POL and RBF). Even though this will merely provide a coarse parameter search, it is definitely better than just keeping the default settings $C = 2^0$ and $\gamma = 0.01$. Overall, 40 different kernel and parameter configurations are checked for the best possible configuration, in particular, four LIN for C , 16 POL for C and γ , 16 RBF for C and γ , and four SIG for C .

As for the RF classifier, we employ Breiman's implementation [74], where the best number of trees within the forest is searched from 50 to 100 in the order of magnitude steps. In each tree, a splitting decision is made in every node based on a randomly sampled number of input features. This number is commonly determined by the square root of the total input features $\sqrt{N_{in}}$. We further add another step between $\sqrt{N_{in}}$ and all features $N_{in}, 1/2(\sqrt{N_{in}} + N_{in})$ which is slightly higher than half of N_{in} . Thus, for each forest size, we also search for the best random split from $\sqrt{N_{in}}$ and $1/2(\sqrt{N_{in}} + N_{in})$.

All configurations are enumerated with a hash function, which basically ranks the configurations with respect to their complexity, e.g., associates higher hash indexes to an individual RF with a higher complexity. This means that while sequentially searching for the best parameters/configurations for any classifier type, it will always favor less complex configurations as long as they realize one of the lowest validation errors during training. It is not our main goal to tweak and achieve best possible classification accuracies for each individual classifier—rather to illustrate the effects of additional features and input sizes of the different classifiers.

During the experiments, the classification tasks conducted over our PolSAR images are considered as uni-class where one sample can only belong to one class, hence during the training phase each positive sample of an individual class can be used as a negative sample for all others. Yet if there are a large number of classes, an unbalanced numbers of positive and negative samples/class may cause the bias problem, i.e., for every positive sample; there will be a large number of negative samples, which may bias the classifier. To prevent this, a negative sample selection is performed in such a way that for each positive sample, the number of the negative samples will be limited according to a predetermined positive-to-negative ratio (PNR). Selection of the negative samples is performed concerning the closest proximity to the positive sample hence the classifier can be trained by discriminating those negative samples (from the positive sample) that have the highest potential for a false-positive. Therefore, if properly trained, the classifier can draw the best possible boundary between the positive and (PNR number of) negative samples, which shall in turn improve the classification accuracy. We use PNR, $PNR = 10$, for negative feature selection for all classifiers whenever needed.

B. PolSAR Images

For our experiments and evaluation, we select three PolSAR images from an airborne system (NASA/Jet Propulsion Laboratory AIRSAR) and a spaceborne system (Canadian Space Agency RADARSAT-2). The AIRSAR supports (full) polarimetric modes for C, L, and P-bands where we focus on the L and C-bands; and RADARSAT-2 works in C-band also supporting the full polarimetric mode. The three selected PolSAR images are from two different areas, such as, Flevoland, Netherlands, and the San Francisco Bay Area (SF Bay), California, USA. We consider this setup to demonstrate how effective the additional color features are over a variety of PolSAR images in terms of the system (AIRSAR

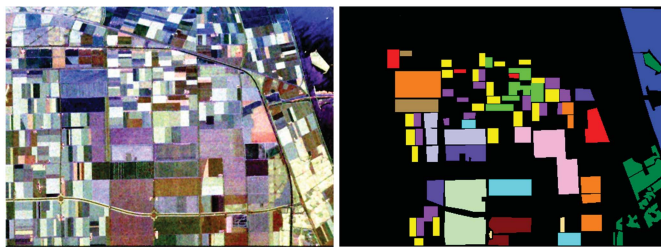
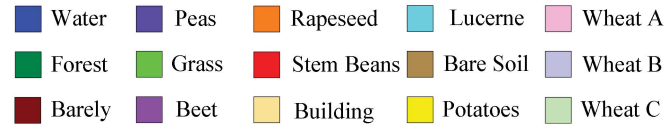


Fig. 6. AIRSAR L-band Flevoland, Pauli color-coded image (left) and used ground truth (right). Class legend for ground truth on top.

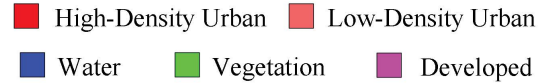


Fig. 8. RADARSAT-2 San Francisco 2008 C-band, Pauli color-coded image C-band (left) and used ground truth (right). Class legend for ground truth on top.

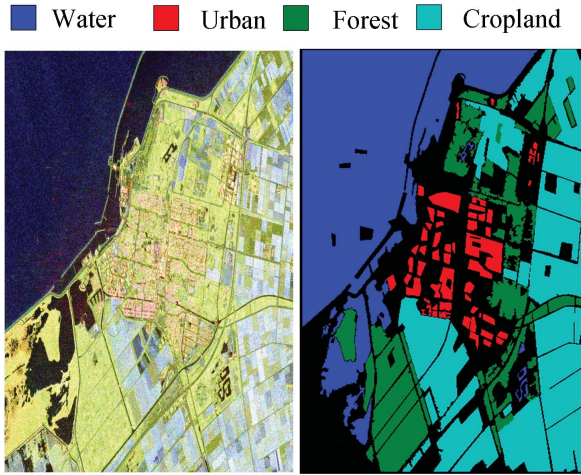


Fig. 7. RADARSAT-2 C-band Flevoland, Pauli color-coded image (left) and used ground truth (right). Class legend for ground truth on top.

and RADARSAT-2), the operative band (C and L), and the underlying classification problem (e.g., number of classes and terrain types).

1) *Flevoland, AIRSAR, L-Band:* The four-look fully polarimetric L-band data of Flevoland, The Netherlands, was collected in mid-August 1989 during MAESTRO-1 Campaign with a size of 1024×750 pixels and a resolution of $\sim 12 \times 6$ m. This particular region is extensively used as a test side for crop and land classification over the past years with well-established ground truth data [4] of 15 classes as shown in Fig. 6.

2) *Flevoland, RADARSAT-2, C-Band:* This RADARSAT-2 fully PoLSAR image at one quad-pol mode (10×5 -m resolution) of Flevoland, The Netherlands, was taken in April 2008. The selected scene is a $\sim 1600 \times 2400$ -pixel subregion, which mainly contains four terrain classes: 1) *woodland/forest*; 2) *cropland*; 3) *water*; and 4) *urban area* [24] with an emphasis on natural and agricultural terrain. The Pauli color-coded image and the ground truth data are shown in Fig. 7.

3) *SF Bay, RADARSAT-2, C-Band:* The area around the bay of San Francisco with the golden gate bridge is probably one of the most used scenes in SAR classification over the past decades. It provides a good coverage of both natural (e.g., sea, scrubs, and forests) and man-made targets (e.g., buildings, streets, parks, and golf course). As no real

ground truth data by on-site visits is available, we generate the ground truth data by visually inspecting radar and optical data as well as using the USGS National Land Cover Dataset (NLCD) 2006 [78]. We identify three major terrain classes such as: 1) *water*; 2) *man-made*; and 3) *vegetation* with the major emphasis on *man-made* terrain type, which may be further divided into: 1) *developed*; 2) *high-*; and 3) *low-density urban* areas depending on their mixture with other natural terrain. Therefore, the ground truth accuracy cannot be 100% guaranteed. For instance, the different man-made classes may also cover trees (planted alongside roads or gardens of houses), thus classification is performed by considering the majority terrain type.

This RADARSAT-2 fully PoLSAR image at fine quad-pol mode (10×5 -m resolution) of SF Bay was taken in April 2008. The selected scene is an $\sim 1400 \times 1800$ -pixel subregion, which contains mainly five classes: 1) *water*; 2) *vegetation*; 3) *developed*; 4) *high-*; and 5) *low-density urban*. The Pauli-coded pseudocolor image and the used ground truth data is shown in Fig. 8.

In total, we have three different PoLSAR images, considering different locations, sensors, and bands. Table II shows a summary of the used polarimetric image data for our experimental setup as well as the abbreviations used for the remainder of this paper.

With this ground truth data, we adapt the following procedure to generate the training and testing sets for each PoLSAR image. For training, we select ~ 100 pixels/class for the lower resolution AIRSAR image and ~ 500 pixels/class for the larger RADARSAT-2 images. For the testing sets, we either select 50,000 pixels/class or the entire class ground truth if its size is $< 50,000$. The reason for this is that we try to keep a training-to-testing ratio between 1:100 and 1:120 for all PoLSAR images and also assure that the training and testing sets are of similar sizes for the individual PoLSAR images. In addition, the training data is split into 50% for training and 50% for validation; and Table III shows a summary of the used training and testing data per PoLSAR image. All PoLSAR images are

TABLE II

OVERVIEW OF POLARIMETRIC IMAGE DATA USE WITHIN EXPERIMENTS

Name	System + band	Abbr.	Date	Incident angles
Flevoland	AIRSAR L	<i>Flevo_L</i>	Aug 1989	40-50°
Flevoland	RADARSAT-2 C	<i>Flevo_C</i>	Apr 2008	30°
SF Bay	RADARSAT-2 C	<i>SFBay_C</i>	Apr 2008	30°

TABLE III

POLARIMETRIC IMAGE DATA AND THEIR TRAINING AND TESTING SETS FOR CLASSIFICATION EXPERIMENTS

Abbr.	Dimensions	#class	Train Size	Test Size
<i>Flevo_L</i>	1024x750	15	1793	208186
<i>Flevo_C</i>	1639x2393	4	2000	200000
<i>SFBay_C</i>	1426x1876	5	2500	250000

TABLE IV

COMBINATIONS OF POLSAR AND IMAGE PROCESSING FEATURE VECTORS USED IN CLASSIFICATION EXPERIMENTS

Feature set	Feature vector	Size	Description
FS ₁	FV ₁	12	Elements from $\langle [T] \rangle$ and $\langle [C] \rangle$
FS ₂	FV ₂	11	Components of H/a/A and eigenvalue decomposition, RVI
FS ₃	FV ₁ +FV ₂	23	Combination of FS ₁ and FS ₂
FS ₄	FV ₃ +FV ₄ +FV ₅	23	Components from target decompositions (Pauli, Krogager, Touzi, Freeman3, Huynen; VanZyl3, and Yamaguchi4)
FS ₅	FV ₁ +FV ₃ +FV ₄ +FV ₅	35	Combination of FS ₁ and FS ₄
FS ₆	FV ₁ +FV ₂ +FV ₃ +FV ₄ +FV ₅	46	Combination of FS ₃ and FS ₄
C	FV ₁₀ +FV ₁₁ +FV ₁₂	60	Extracted color features
T	FV ₆ +FV ₇ +FV ₈ +FV ₉	81	Extracted texture features

speckle filtered using the suggested filter by Lee [79] with a 5×5 window before any feature is extracted.

C. Features

The extracted PolSAR features from Section II-A, such as FV₁-FV₅, are combined into six different PolSAR feature sets (FS) as shown in Table IV, including basic backscattering information in form of covariance and coherency matrices as FS₁, commonly used components of H/a/A and eigenvalue decomposition as FS₂, and several coherent and incoherent TDs as FS₄, as well as combinations of these. Additionally, each PolSAR feature set is also combined with three sets of visual features based on the features from Section II-B, such as FV₆-FV₁₂. These features are further joined to form a set of color features (FV₁₀+FV₁₁+FV₁₂), C, and a set of textural features (FV₆+FV₇+FV₈+FV₉), T, see bottom of Table IV, hence each FS_x will be augmented by color (FS_x^C), texture (FS_x^T), and color + texture (FS₆^{CT}). Thus, this will result in a total of 24 feature set combinations with various sizes from the smallest ($|FS_2|$) with length 11 and the largest ($|FS_6^{CT}|$ with length 187). We introduce the symbol FS_x^z to abbreviate different groups of feature

set combinations such as FS_x^C for the color combinations of all six different PolSAR feature sets and FS₆^z when referring to all combinations and extensions of the PolSAR feature set FS₆. With this setup of feature set combinations, we can investigate the influence of color and texture as an addition to different selections of PolSAR features.

Regarding the feature dimensions when the number of (representative) training samples is relatively small with respect to the number of features, the well-known problem of the curse of dimensionality (i.e., the Hughes phenomenon) occurs. This results in the risk of overfitting of the training data and can lead to poor generalization capabilities of the classifier. Generally, neither RF nor SVM topologies have a serious curse of dimensionality problem for features of few hundred dimensions. Particularly SVMs with RBF kernel can theoretically learn in infinite dimensions providing that the training data set size is infinite too. Under the light of this, the investigation on curse of dimensionality over the classification performance is beyond the scope of the section and paper as there are excellent research works [80] in the literature.

IV. EXPERIMENTAL RESULTS AND EVALUATIONS

We will first discuss general observations related to the six PolSAR feature sets and the three PolSAR images before going in-depth analysis for each of the individual classification experiment performed.

All the presented results for a different classifier, feature set, and image combination, are average values obtained over multiple runs. We apply the trimmed mean over 12 runs per combination, leaving out the minimum and maximum values to reduce the effects of extreme outliers. First, the average classification accuracies for the six different PolSAR feature sets (and their respected texture and color combinations) over all classifiers and images are shown in Fig. 9 (left) so as to provide an assessment of utilizing texture and color features in combination with the different PolSAR features. As anticipated, the minimal FS₁ benefits highly from texture and color information with large gains of 6% and 15% because of the small discrimination power with just $\langle [C] \rangle$ and $\langle [T] \rangle$ elements. This can also be seen for all the other feature sets FS₂-FS₆, where with the application of more discriminative PolSAR features in form of TDs, the classification accuracies can be increased on the average by $\sim 10\%$, from 77% to 87%. Texture features help to further improve by an extra 1% on the average and the color features can boost that to an additional 3%-5% on the average, to over 90% compared with the PolSAR features. It can be observed that the presence of texture features in FS_x^{CT} have a marginal influence on the classification accuracies compared the color features alone, FS_x^C. Anyhow, also overall differences among the feature combinations for FS₂^z, FS₄^z, FS₅^z, and FS₆^z are not significant, which probably demonstrates why the Cloude-Pottier decomposition (FS₂) is used so extensively. The drop for FS₃ compared with FS₂ comes from the addition of FS₁ and its rather low classification performance. The features of FS₂ are not able to compensate this negative effect. The same observation can be made for FS₅ and FS₆, where the drop is however much smaller as the features and dimensions of FS₅ can better compensate for FS₁.

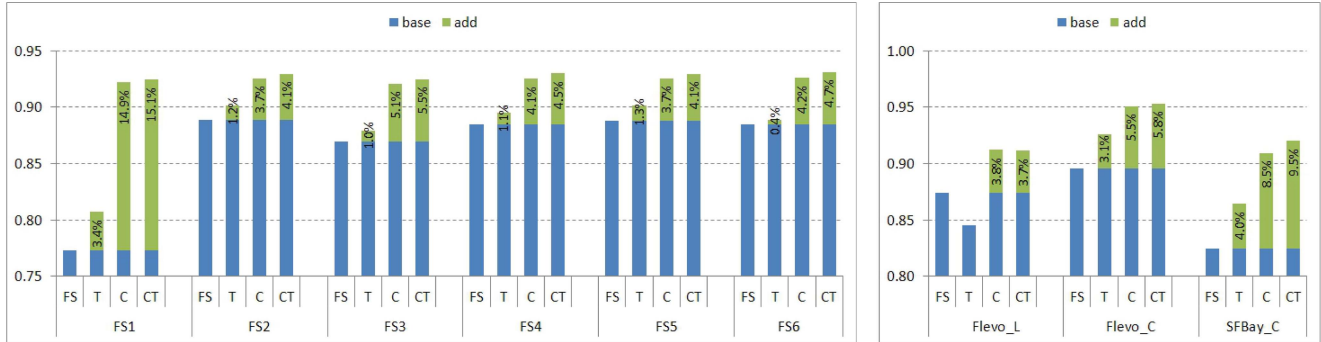


Fig. 9. (Left) Average classification accuracies for the six different feature sets over all classifiers and data sets. (Blue: the base line accuracies of the SAR feature set and green: the improvement with the additional texture and/or color features). (Right) Average classification accuracies for the three different data sets over all classifiers and feature sets.

Second, the average classification accuracy for the three different PolSAR images over all classifiers and feature sets are shown in Fig. 9 (right). It can be clearly observed that for all three images used in these experiments, color features provide an increase in the classification accuracy from 4% to 9%.

Considering *Flevoland_L*, the classification accuracy drops (almost -3%) with the addition of the textural information to FS_x and also the differences between FS_x^C and FS_x^{CT} are fairly marginal. The reason for this is that the texture information has a rather minimal effect on the classification accuracies probably because of the lower resolution of the data and the majority of classes are agriculture fields with no individual prominent texture features.

For the *Flevoland_C* image, the texture features provide some contribution to the classification accuracy and we will see later in the more detailed analysis for this image that primarily the *urban* class accounts for this gain, whereas with the color features a gain of $2.5\%-5.5\%$ compared with FS_x^T/FS_x can be achieved. The classification results with the combination of color and texture is pretty much the same as the one with color alone.

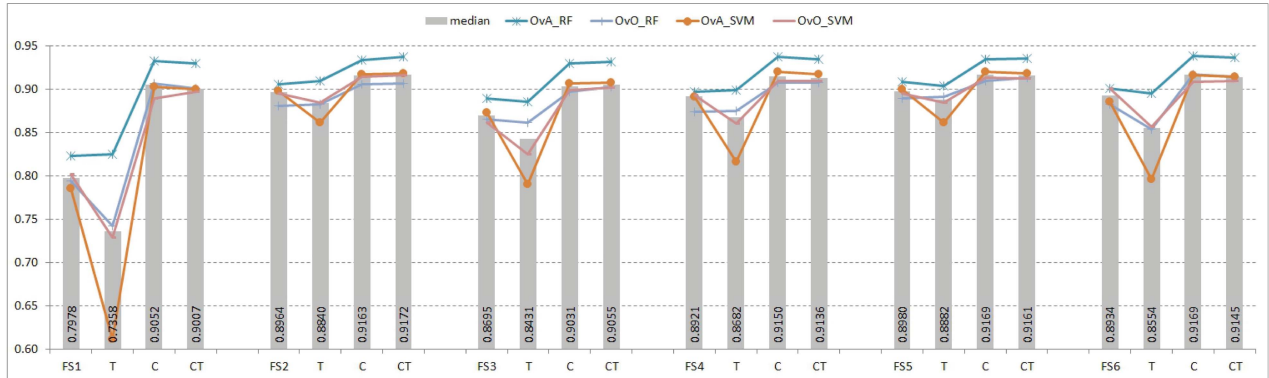
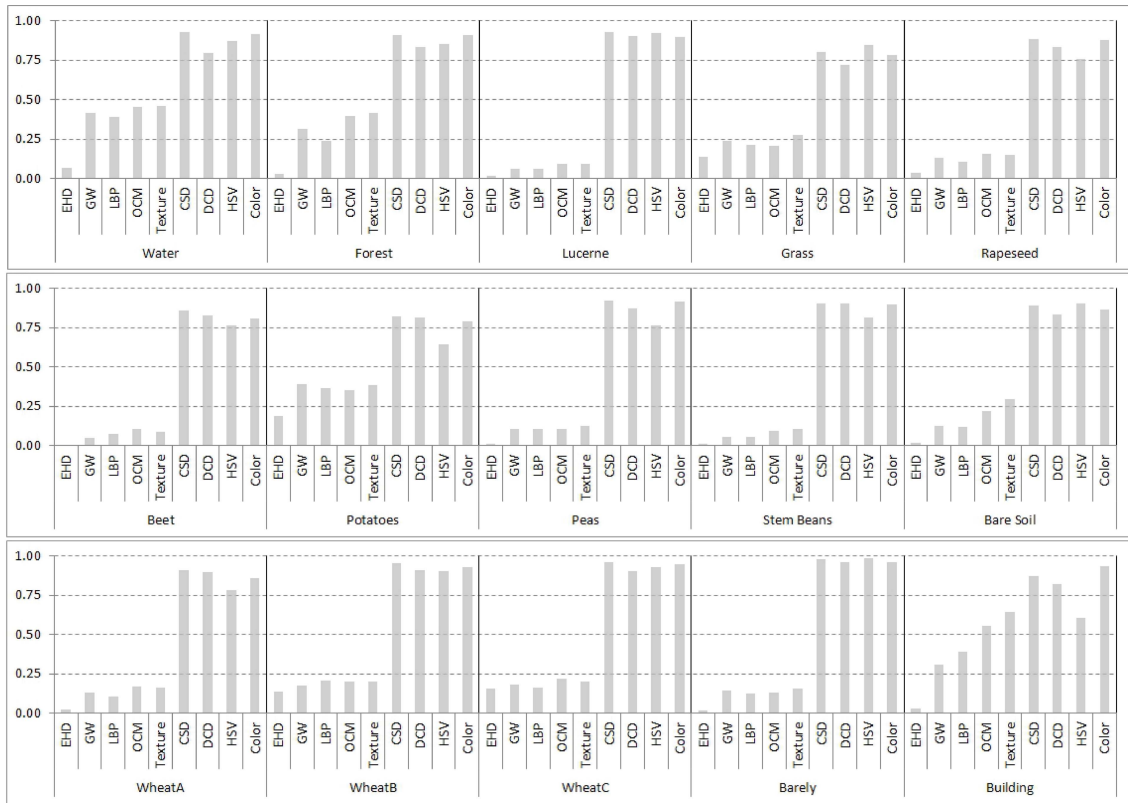
As for the third image, *SFBay_C*, the addition of texture features provides a contribution of $\sim 4\%$ to the overall classification accuracy. On the other hand, the addition of the color features increases the accuracy by $4.5\%/8.5\%$ compared with FS_x^T/FS_x . Thus, whenever the color features are utilized, the contribution of the additional texture features becomes in general less significant, only a 1% improvement for all tested images.

With these observations, we will now have a deeper analysis for each of the individual PolSAR images regarding the different feature sets and how they affect individual classes. The classification accuracies for the images and their classes are visualized through box plots. We have chosen them as an effective way for representing graphically a large amount of numerical data. They depict five values, such as the least observation (here, it is the minimum accuracy), lower quartile (25%), median, upper quartile (75%), and the highest observation (maximum accuracy). As observed in the previous results, Fig. 9, all feature sets besides FS_1^z show similar behavior and tendencies with the additional color and texture features. Therefore, all box plots for an individual image are gener-

ated over all classifier runs for a particular feature set (e.g., $FS_2^T-FS_6^T$) applying some basic outlier removal for the extreme cases where a particular classifier run performs significantly different from the others. This mainly removed outliers from the bottom end of the accuracy range.

1) *Flevoland, AIRSAR, L-Band*: The main observation for the *Flevoland_L* image in Fig. 10 is the loss of accuracy for the FS_x^T feature sets for individual classifiers. The performance of SVM seems to be varying with respect to the multiclass topology, i.e., the OvA_SVM shows heavy drops for each FS_x^T ; and the performance of OvO_SVM also drops to or below the median and being among the lowest accuracies for the majority of FS_x^T . It can be observed that three out of four classifier performances are severely affected by texture especially for FS_1^T , FS_3^T , and FS_6^T , which also include FV_1 (i.e., $\langle [C] \rangle / \langle [T] \rangle$ elements) and cannot provide good discrimination in this classification task. This is probably because of the fact that SVM work on the entire feature set and, obviously, the texture has quite a negative effect particularly on the large number of classes (15) in this image. OvA_RF is the most invariant to FS_x^T as RF employs random feature selection within each ensemble decision tree, hence, not suffering from the lower discrimination of FV_1 and the texture features. However, we can observe that RF is quite affected by the OvO multiclass topology because of its pairwise classification. Here, OvA_RF performs significantly better than its OvO counterpart as well as the two SVM classifiers.

The effect of the texture and color features can be closer investigated in Fig. 11, which shows the results for the single and combined texture and color features per class for *Flevoland_L*. We can observe that overall the texture features perform rather poorly, where 1) *water*; 2) *forest*; 3) *potatoes*; and 4) *building* are exceptions in the sense that texture features obtain results three to four times better than the other classes. In addition, the single GW and OCM feature achieve best results and are also the main contributor to the combined texture feature for these four classes. For the other classes, texture feature discrimination does virtually not exist, hence they cannot provide any significant additional discrimination when combining with the extracted PolSAR features in this *Flevoland_L* classification task. Regarding the color features, results look more positive with single and combined color features able

Fig. 10. Average classification accuracies for the four classifier topologies per feature set over *Flevo_L* image (gray bar: the median value).Fig. 11. Classification accuracies for the *Flevo_L* classes over the single and combined texture and color features.

to obtain better results and in this particular case outperform their texture counterparts, which is also reflected in the results when combined with the PolSAR features.

Overall, the introduction of the texture features have either an insignificant or rather negative effect, which is also visible in the box plots for FS_x^T in Fig. 12, where lower quartile (25%) and upper quartile (75%) rectangles are far larger indicating a higher variation in accuracies compared with the more compact representations for the other feature sets (also Fig. 12). As discussed earlier, this is probably due to the larger number of classes, majority of which being agriculture fields, thus no significant texture difference exists among them. In addition, such a low-resolution SAR data may not allow for major textural discriminations and, in addition, the applied speckle filtering may further degrade the texture information. Therefore, such a degraded and somewhat similar texture

information among most of the classes rather introduce confusion and makes it difficult to learn individual class patterns when the majority of features are quite similar and noisy for a large number of different classes as shown in Fig. 11. Recall that the texture features have an overall dimension of 81 compared with the PolSAR features having dimensions between 10 and 40 for different FS_x^T ; hence texture will have a rather dominating influence. RF can better cope with this effect than SVM as a small number of features are randomly selected within each tree in the forest, which in turn, will negate the influence of the large texture feature dimension. Yet, the differences for FS_x^C and FS_x^{CT} are not as significant as for FS_x^T besides some variations with respect to whisker ranges. This means that the color features carry the main discrimination information and can cancel out negative effects from the texture features.

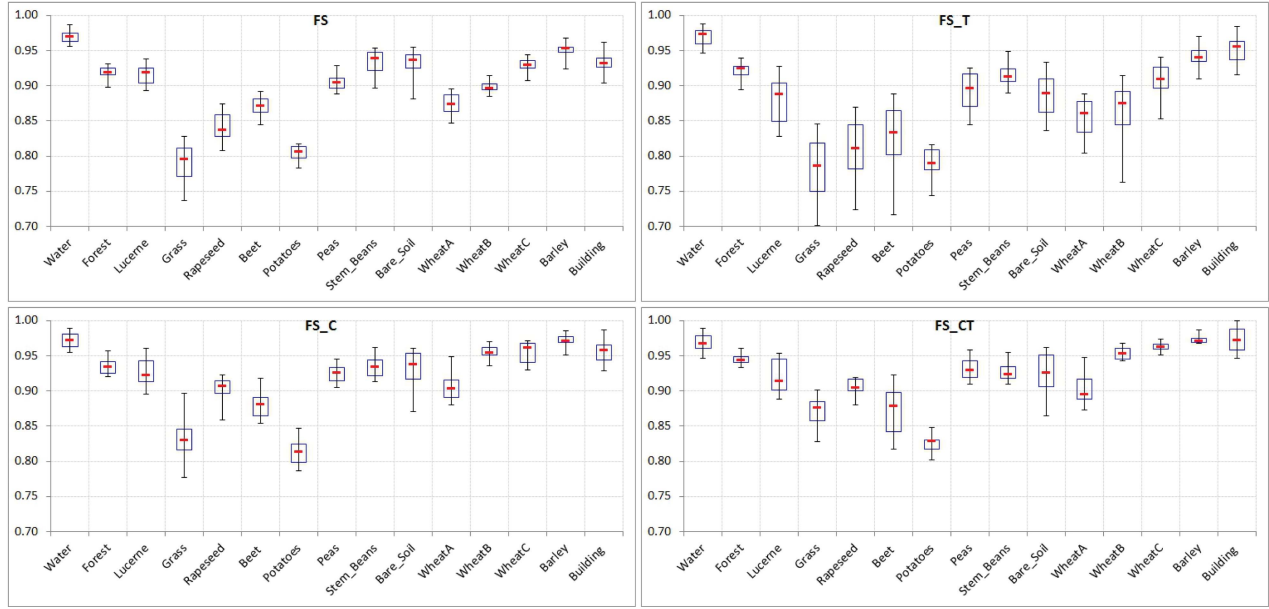


Fig. 12. Classification accuracies for the *Flevo_L* classes with FS_x (left), FS_x^{CT} (right) in top row and FS_x^C (left), FS_x^{CT} (right) in bottom row. Box plots: 25% and 75% percentile as the blue rectangle. Red line: the median. Whiskers: the min. and max. values, respectively.

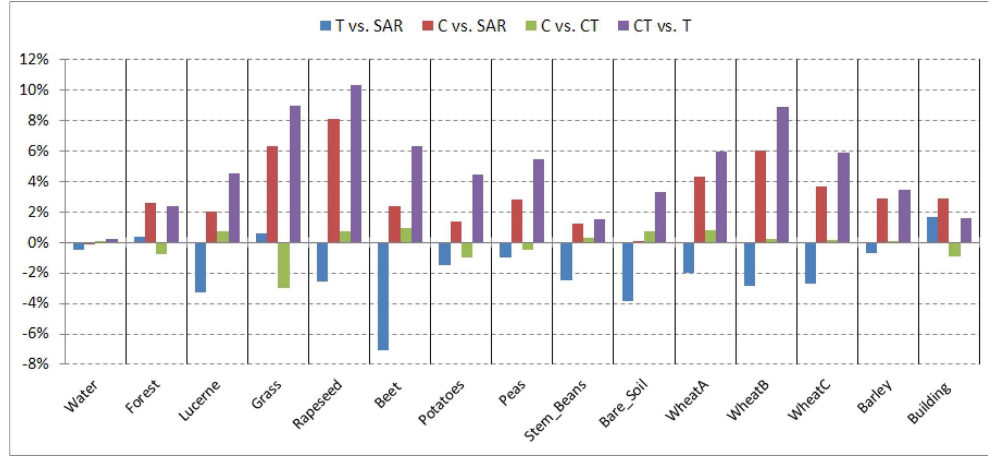


Fig. 13. Differences in classification accuracies comparing the influence of texture and color features per class in the *Flevo_L* image.

A better visualization of the feature differences are shown in Fig. 13, which shows classification accuracy gains/losses per terrain class. Only for the *building* class texture makes a noticeable yet marginal positive impact (1%). For the other 14 classes, 12 of them suffer in accuracy with the addition of texture features because of the absence of strong textural pattern to provide significant discrimination. For the addition of color features, two classes gain $\sim 1\%$ accuracy and the majority of eight classes gain between 2% and 4%. Highest impact for classes *Grass*, *Rapeseed*, and *Wheat B*, which gain $>6\%$ in accuracy compared with just PoLSAR features (FS_x).

Fig. 14 shows the classification results for the *Flevo_L* image showing the differences of just PoLSAR features (FS_3) versus its augmented feature sets with texture, color, and texture + color, respectively, for the OvO_SVM classifier. For the FS_3^T case, the larger drops for *Beet* and *Bare_Soil* class are clearly visible, whereas for the classes with drops of 2% or lower, differences are not as visible. It is noticeable that

the *forest* area on the small island is slightly better classified as for FS_3 , particular around the borders. As for FS_3^C , visual differences to FS_3 and FS_3^T are noticeable in particular for the classes that have shown larger numerical improvements in Fig. 13.

2) *Flevoland, Radarsat-2, C-Band*: Compared with the *Flevo_L* image, in Fig. 15 texture features have a more positive impact, as no severe drops exist for FS_x^T and they rather improve the classification accuracies compared with FS_x . Yet, the color features in FS_x^C are able to provide a better discrimination to further improve classification results. With the combination of texture and color features, both RF classifiers can actually increase their classification accuracies from FS_x^C to FS_x^{CT} whereas SVM either drop (FS_2^{CT} – FS_5^{CT}) or stay around level (FS_1^{CT} , FS_6^{CT}) with their respective FS_x^C results.

As observed in Fig. 15, texture features provide additional discrimination power to improve classification accuracies

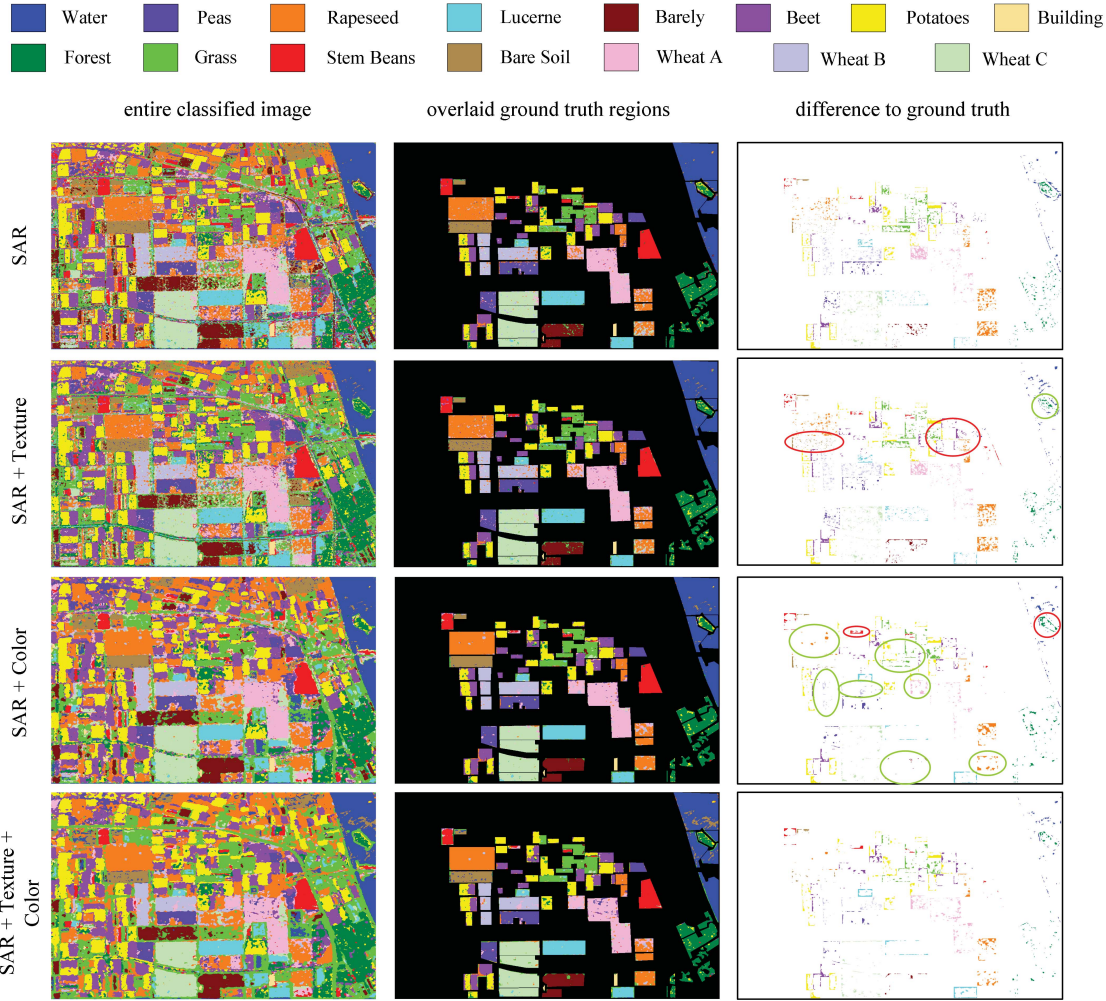


Fig. 14. Classification results for the *Flevo_L* image for FS_3 over OvO_SVM. First column: classified SAR image, the second column: classified image overlaid with the ground truth, and the third column: difference of GTD to the second column with the color indicating what the ground truth should be. Circles: degradation (red) and improvement (green). First row shows results: FS_3 , the second row: FS_3^T , the third row: FS_3^C , and the last row: FS_3^{CT} .

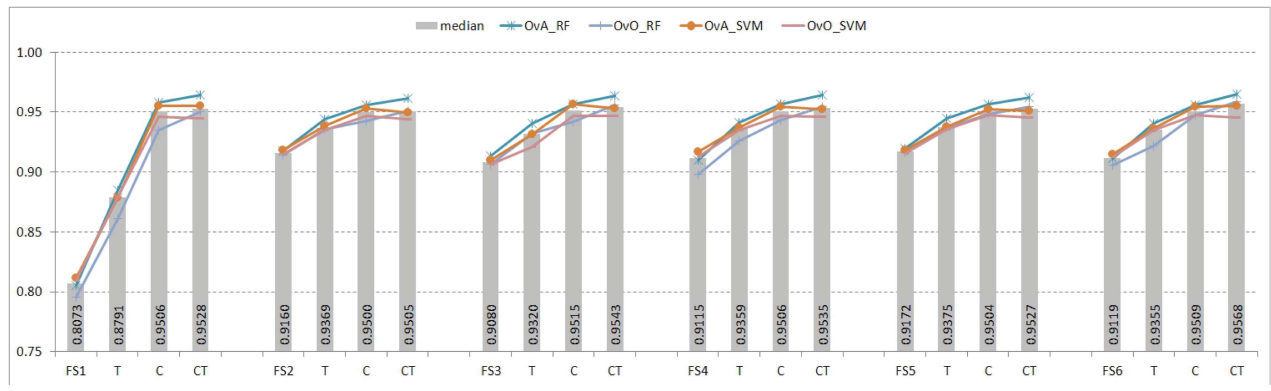
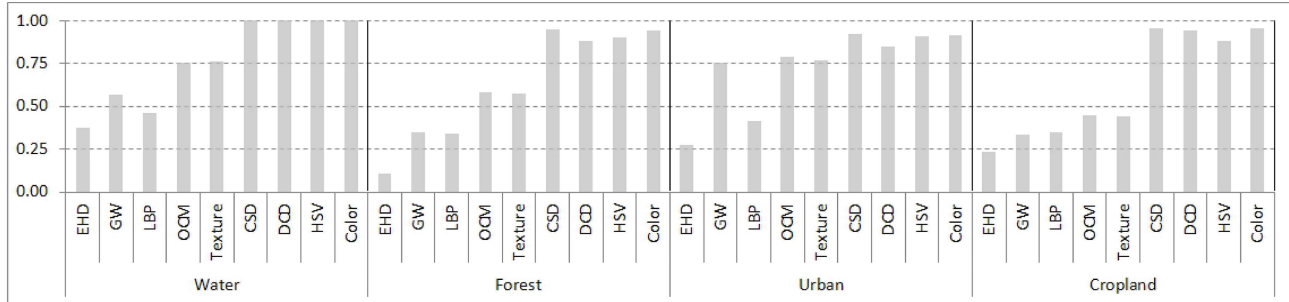
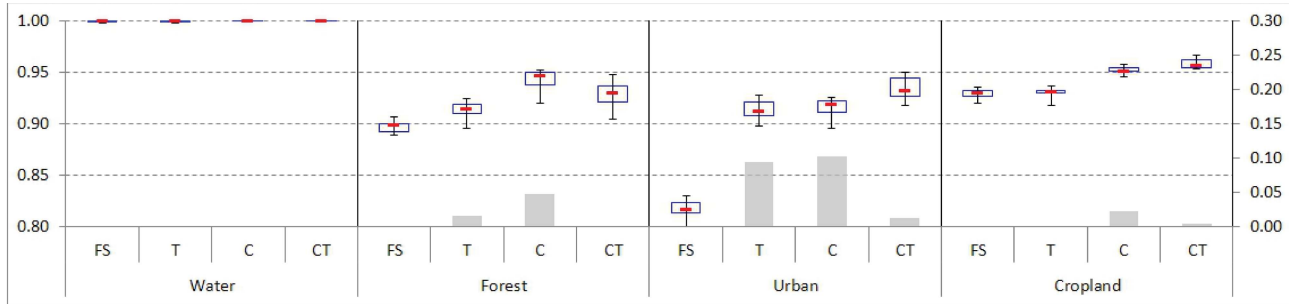


Fig. 15. Average classification accuracies for the four classifiers per feature set over *Flevo_C* image (gray bar: the median value).

with particularly *water* and *urban* obtaining good results with texture features alone as well as for *forest* even though not quite as good as for the previous two terrain classes as shown in Fig. 16. On the contrary, the *cropland* class does not seem to carry any significant texture patterns; however, the color features seem to provide a better discrimination for this terrain class.

From the box plot in Fig. 17, the different box plot shapes and values are close together and the minimum and maximum values are not too far off from the main quartile body, so as there is not too much variance within the different classifiers. When investigating the effect of particular feature sets for individual classes, it is revealed that the increase of FS_x^T accuracy in Fig. 15 appears primarily from the *urban*

Fig. 16. Classification accuracies for the *Flevo_C* classes over the single and combined texture and color features.Fig. 17. Classification accuracies for the *Flevo_C* classes and differences in classification accuracy comparing the influence of texture and color features per class. The box plots: 25% and 75% percentile as the blue rectangle, the red line: the median, and whiskers: min. and max. values, respectively, with accuracies on the primary axis on the left. The gray bars: the feature accuracy differences with the secondary axis on the right.

class with an improvement $\sim 9.5\%$ and this is actually the only one that significantly gains from the texture features because of the unique patterns of roads and buildings. This can also be seen when visually inspecting the image where the majority of classes do not really have a strong texture pattern besides the *urban* class. Even though reasonable results with texture features can also be obtained for *forest* (60% as seen in Fig. 16), they do not seem to add as much additional discrimination to the FS_x . The same observation can be made for *cropland* over the color features with FS_x^C similar to FS_x^T and marginal improvements for FS_x , which already achieves high classification accuracy. *Forest* and *urban* are the classes that highly benefit from the additional color features with 5% and 10% accuracy gains compared with PoLSAR features only, where FS_x^C and FS_x^T perform equally for the *urban* class. Additional color and texture features have no effect on the classification accuracy of *water*, for which the PoLSAR features already provide the highest possible discrimination against the other classes because of its dominant surface scattering.

Fig. 18 shows classification results for the *Flevo_C* image showing the differences of PoLSAR features alone (FS_2) versus its augmented feature sets for the OvA_RF classifier with texture, color, and texture + color, respectively. For the FS_2^C case, the numerical improvements in the urban areas are also noticeable visually. However, in the classified image it tends to overestimate the *urban* area as well as misclassifies edges between *forest* and *water* or other flat areas most probably because of feature extraction over the pixel neighborhood. It also misclassifies some *water* regions as visible in the bottom right part. On the contrary, the FS_2^C classifies those *water* regions correctly and does not suffer from the *forest/water*

borders. The improvements on the classification performance for FS_2^C are visible, too. In addition, for this feature set *forest* and *cropland* areas in the bottom left and right of the image are classified to the level closer to the ground truth than for FS_2 and FS_2^T .

3) *SF Bay, RADARSAT-2, C-Band*: The behavior of the classifiers, as shown in Fig. 19, is different compared with the two previous images. The texture features provide good discrimination improving the FS_x accuracies by $2\%-3\%$ compared with FS_{2-6} and 9% compared with FS_1 , whereas the color features are able to provide an additional improvement of $3\%-4\%$ and 10% compared with FS_{2-6}^T and FS_1^T , respectively. In addition, for this particular image, the texture features are able to provide, though small, additional discrimination when combined with the color features. These tendencies are visible for all classifiers as observed distinctively for the two Flevoland images.

The OvA versions of RF and SVM perform at the top level; however, the OvO topology classifiers perform on a just slightly lower level within a maximum margin 4% difference for FS_x^T and $1\%-3\%$ for the others, where OvO_RF accounts for the majority of the larger 4% gaps.

The classification accuracy of the *water* class stays constant (Fig. 21) because of its unique single-bounce backscattering discrimination, whereas the other classes are scatter mixtures of double-bounce and volume scattering. For other classes, the texture features have a low contribution on *high urban* and *vegetation* classes with $\sim 2\%$ and larger influence with 3% and 6% for *low urban* and *developed*, respectively. However, even though the overall classification accuracy gain of the man-made terrain classes is minimal (Fig. 21), the effect of the texture features is still visible with regard to the

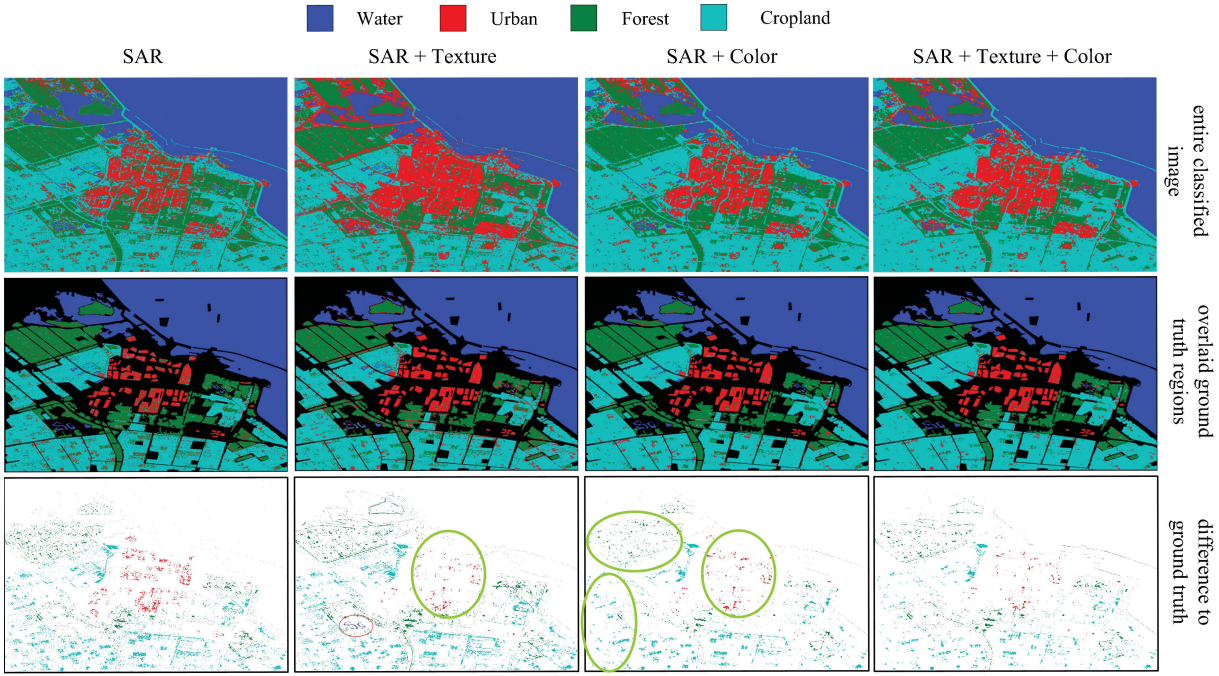


Fig. 18. Classification results for the *Flevo_C* image for FS_2 over Ova_RF. First column: classified SAR image. Second column: classified image overlaid with the ground truth. Third column: difference of GTD to the second column with the color indicating what it should be. Circles: degradation (red) and improvement (green). First row shows results: FS_2 , second row: FS_2^T , third row: FS_2^C , and last row: FS_2^{CT} .

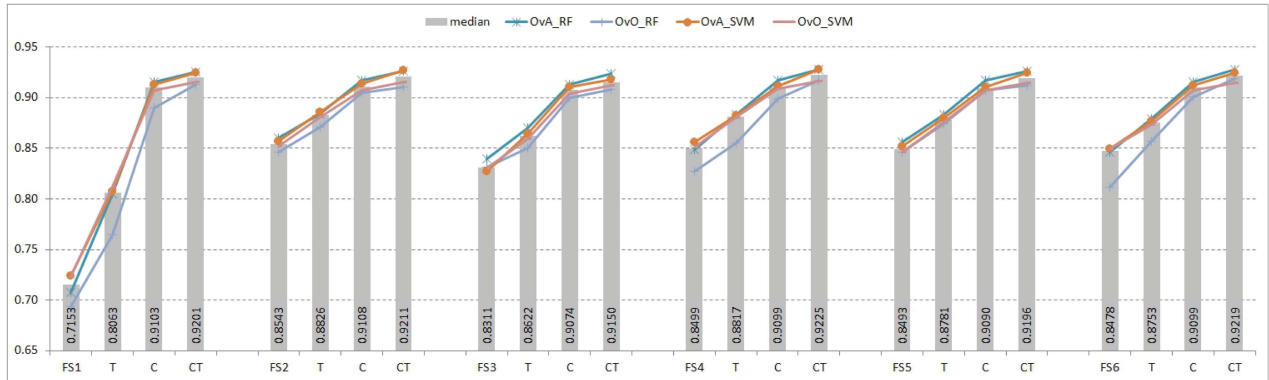


Fig. 19. Average classification accuracies for the four classifiers per feature set over *SFBay_C* image (gray bar: the median value).

box plot shapes showing more variance within FS_x^T than FS_x^C because of the larger quartile body. Anyhow, the color features have varying contributions from lower 2% for *vegetation*, to significant higher 7% for developed, and 10% for the two urban classes, *high urban* and *low urban*. Evidently even though the man-made terrain classes have textural patterns (roads and buildings), as visible in the results of the single-texture features in Fig. 22, differences among these classes are not discriminated enough by the texture features as they are by the color features.

This is further visible in Fig. 22, which shows the classification results for the *SFBay_C* image for the OvA_SVM classifier showing the differences of PolSAR features (FS_5) versus its augmented feature sets with texture, color, and texture + color, respectively. In the FS_5^T case, it is capable of providing better results of the *water* region around the bridge on the right-hand side of the image. In addition, the improvements in the classification of the developed and of the

low-urban areas are visually noticeable compared with FS_5 in the graph of Fig. 21. However, only parts of the *low-urban* areas on the left side of the image show better classification results whereas the area in the bottom right corner is only slightly affected. On the other hand, the classifier with FS_5^C achieves better performance for all larger *low-urban* areas as well as the *developed* and *high-urban* regions on the right-hand side.

Overall, when evaluating individual classes in all PolSAR image data set used, *water* is the least affected by the addition of texture or color features because of the aforementioned reasons. *Forest* or main treelike *vegetation* benefited from color more with ~2%–5% whereas with texture it is ~1%–3%. In this regard, man-made terrain classes such as urban areas profit the most because of their underlying surface characteristics, hence for the *Flevo_C* and *SFBay_C* images, they could gain up to 10% reaching or exceeding 90% level in classification accuracy.

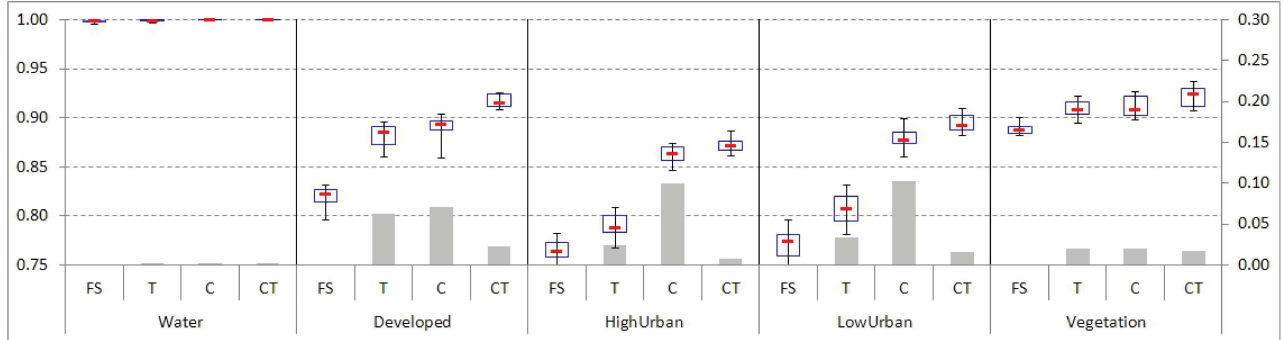


Fig. 20. Classification accuracies for the *SFBay_C* classes and differences in classification accuracy comparing the influence of texture and color features per class. Box plots: 25% and 75% percentile as the blue rectangle. Red line: the median. Whiskers: min. and max. values, respectively, with accuracies on the primary axis on the left. The gray bars: the feature accuracy differences with the secondary axis on the right.

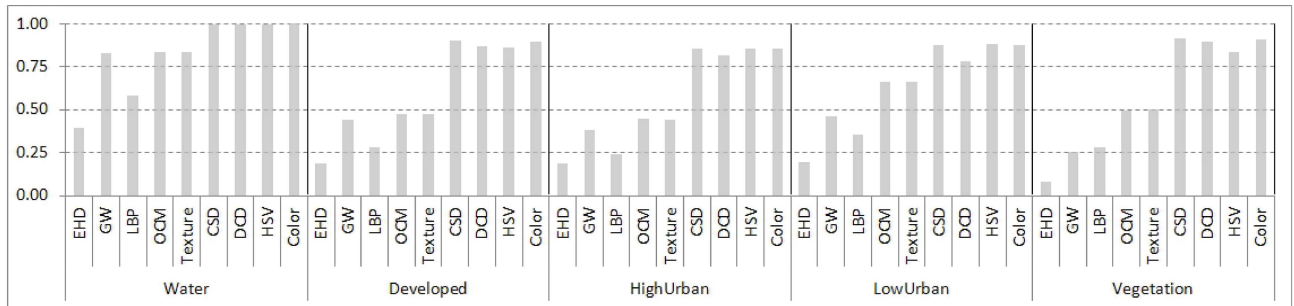


Fig. 21. Classification accuracies for the *SFBay_C* classes over single and combined texture and color features.

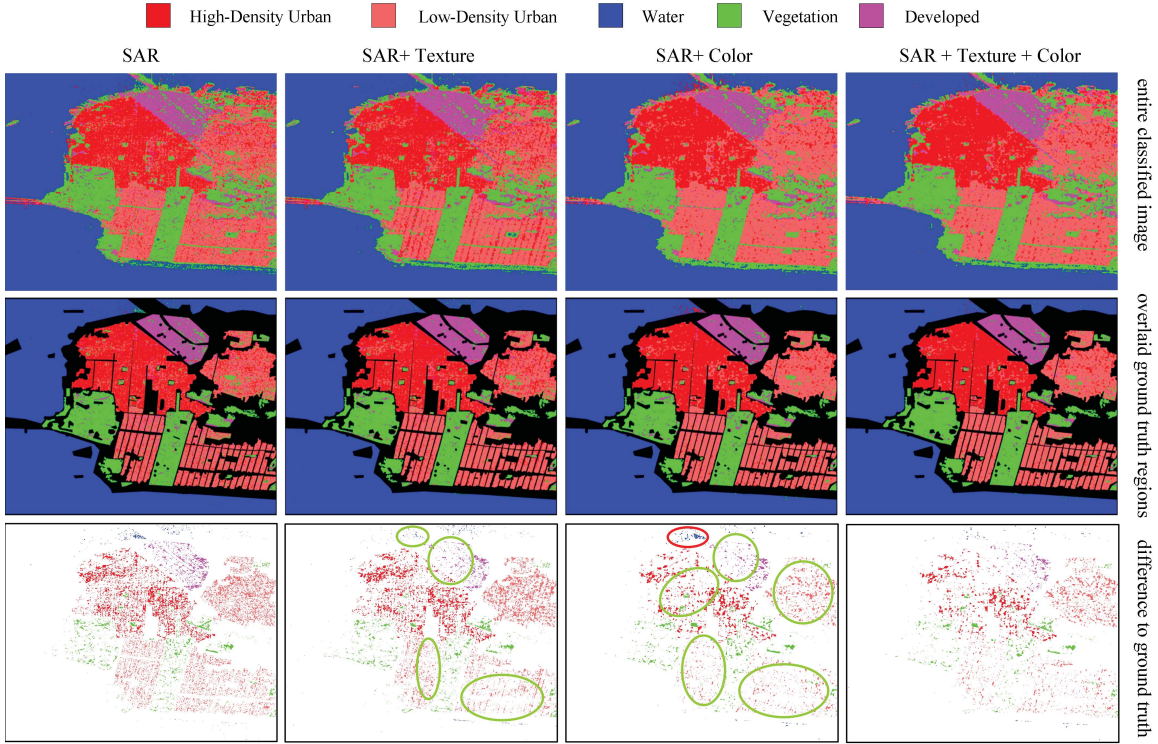


Fig. 22. Classification results for the *SFBay_C* image for FS5 over Ova_SVM. First column: classified SAR image. Second column: classified image overlaid with the ground truth. Third column: difference of GTD to the second column with the color indicating what it should be. Circles mark degradation (red) and improvement (green). First row shows results: FS5. Second row: FS5^T. Third row: FS5^C, and the last row: FS5^{CT}.

Generally, it is evident that with the additional color features higher classification accuracies are obtained. When a certain texture pattern is present within the classes, the texture features

can enhance the classification accuracies; however, vice versa is also possible that when none of the classes have a significant textural pattern, the texture features may rather blur or degrade

discrimination which in turn will cause degradations in the classification performance. On the average, over all experiments, the color features outperform the texture features in terms of classification accuracy improvements in all PolSAR feature combinations.

V. CONCLUSION

In this paper, we investigated PolSAR classification with the extension of color features extracted over a pseudocolor image generated by Pauli color coding in polarization basis (H,V). In our extensive set of experiments, we considered six different PolSAR feature combinations augmented with texture and color features over three PolSAR images from the AIRSAR and RADARSAT-2 systems and evaluated two common classifiers, such as, SVMs and RFs, within two multiclass topologies OvO and OvA.

We observed that the OvA version of RF provided the most stable results with the highest accuracies throughout our tested PolSAR images. The combination of OvA and SVM achieved the second best results, on the average, for the color and texture augmented feature sets, however; results are not as stable considering all feature sets over the Flevoland and SF Bay data sets. According to observations over our various experiments, RF and SVM within OvA can be regarded as viable options as first choice classifiers for PolSAR LULC classification applications considering other factors such as personal preference, complexity, implementation, and possible future applications concerning extensibility and scalability.

The experimental results demonstrated that with the addition of the color features, all classifiers outperformed the results with PolSAR features alone as well as achieved higher classification accuracies compared with the traditional feature combination of PolSAR and texture features. We can conclude that the tested color features applied to the pseudocolor image in the Pauli H, V basis provide further improvements in terms of class discrimination when compared with their texture counterparts. Texture features may still provide valuable discrimination and, as for the color features, the gains and losses achieved will vary with the PolSAR classification problem they are applied to. In our experiments, we observed that the application of the color features to fully PolSAR classification can provide noteworthy improvements in particular, man-made and foliage and tree-type dominated *vegetation* terrain classes highly benefited from the additional color features.

As for the future work, this investigation will be further extended to the dual- and single-polarization modes considering other current airborne and spaceborne SAR systems.

ACKNOWLEDGMENT

The authors would like to thank anonymous reviewers for their help, useful comments, and contribution to this paper's improvement. The authors would also like to thank NASA/JPL for making the POLSAR data publicly available. RADARSAT is an official mark of the Canadian Space Agency. RADARSAT-2 Data and Products MacDONALD, DETTWILER, and ASSOCIATES LTD. (2008)—all rights reserved.

REFERENCES

- [1] J. S. Lee and E. Pottier, "Airborne and space-borne polarimetric SAR systems," in *Polarimetric Radar Imaging: From Basics to Applications*, B. J. Thompson, Ed. Boca Raton, FL, USA: CRC Press, 2009.
- [2] E. Attema, M. Davidson, P. Snoeij, B. Rommen, and N. Flouri, "Sentinel-1 mission overview," in *Proc. IEEE Int. Geosci. Remote Sens. Symp.*, vol. 1, Jul. 2009, pp. 36–39.
- [3] K. Ersahin, I. G. Cumming, and R. K. Ward, "Segmentation and classification of polarimetric SAR data using spectral graph partitioning," *IEEE Trans. Geosci. Remote Sens.*, vol. 48, no. 1, pp. 164–174, Jan. 2010.
- [4] P. Yu, A. K. Qin, and D. A. Clausi, "Polarimetric SAR image segmentation using region growing with edge penalty," *IEEE Trans. Geosci. Remote Sens.*, vol. 50, no. 4, pp. 1302–1317, Apr. 2012.
- [5] F. Del Frate, G. Schiavon, D. Solimini, M. Borgeaud, D. H. Hoekman, and M. A. M. Vissers, "Crop classification using multiconfiguration C-band SAR data," *IEEE Trans. Geosci. Remote Sens.*, vol. 41, no. 7, pp. 1611–1619, Jul. 2003.
- [6] Y. Hara, R. G. Atkins, S. H. Yueh, R. T. Shin, and J. Kong, "Application of neural networks to radar image classification," *IEEE Trans. Geosci. Remote Sens.*, vol. 32, no. 1, pp. 100–109, Jan. 1994.
- [7] K. Chen, W. Huang, D. Tsay, and F. Amar, "Classification of multifrequency polarimetric SAR imagery using a dynamic learning neural network," *IEEE Trans. Geosci. Remote Sens.*, vol. 34, no. 3, pp. 814–820, May 1996.
- [8] Y. Tzeng, "A fuzzy neural network to SAR image classification," *IEEE Trans. Geosci. Remote Sens.*, vol. 36, no. 1, pp. 301–307, Jan. 1998.
- [9] D. H. Hoekman and M. A. M. Vissers, "A new polarimetric classification approach evaluated for agricultural crops," *IEEE Trans. Geosci. Remote Sens.*, vol. 41, no. 12, pp. 2881–2889, Dec. 2003.
- [10] T. L. Ainsworth, J. P. Kelly, and J. Lee, "Comparisons between dual-pol, compact polarimetric and quad-pol SAR imagery," *ISPRS J. Photogramm. Remote Sens.*, vol. 64, no. 5, pp. 464–471, Sep. 2009.
- [11] J. S. Lee, M. R. Grunes, and E. Pottier, "Quantitative comparison of classification capability: Fully polarimetric versus dual and single-polarization SAR," *IEEE Trans. Geosci. Remote Sens.*, vol. 39, no. 11, pp. 2343–2351, Nov. 2001.
- [12] H. Skriver, F. Mattia, G. Satalino, A. Balenzano, V. R. N. Pauwels, N. E. C. Verhoest, and M. Davidson, "Crop classification using short-revisit multitemporal SAR data," *IEEE J. Sel. Topics Appl. Earth Observat. Remote Sens.*, vol. 4, no. 2, pp. 423–431, Jun. 2011.
- [13] C. Chen and K. Chen, "The use of fully polarimetric information for the fuzzy neural classification of SAR images," *IEEE Trans. Geosci. Remote Sens.*, vol. 41, no. 9, pp. 2089–2100, Sep. 2003.
- [14] R. Hänsch, "Complex-valued multi-layer perceptrons—An application to polarimetric SAR data," *Photogram. Eng. Remote Sens.*, vol. 76, no. 9, pp. 1081–1088, Sep. 2010.
- [15] S. R. Cloude and E. Pottier, "A review of target decomposition theorems in radar polarimetry," *IEEE Trans. Geosci. Remote Sens.*, vol. 34, no. 2, pp. 498–518, Mar. 1996.
- [16] W. An, Y. Cui, and J. Yang, "Three-component model-based decomposition for polarimetric SAR data," *IEEE Trans. Geosci. Remote Sens.*, vol. 48, no. 6, pp. 2732–2739, Jun. 2010.
- [17] M. Arii, J. J. van Zyl, and Y. J. Kim, "Adaptive model-based decomposition of polarimetric SAR covariance matrices," *IEEE Trans. Geosci. Remote Sens.*, vol. 49, no. 3, pp. 1104–1113, Mar. 2011.
- [18] A. Sato, Y. Yamaguchi, and G. Singh, "Four-component scattering power decomposition with extended volume scattering model," *IEEE Geosci. Remote Sens. Lett.*, vol. 9, no. 2, pp. 166–170, Mar. 2012.
- [19] L. J. Du and J. S. Lee, "Polarimetric SAR image classification based on target decomposition theorem and complex Wishart distribution," in *Proc. IEEE Int. Geosci. Remote Sens. Symp.*, vol. 1, May 1996, pp. 439–441.
- [20] M. Hellmann, G. Jager, E. Kratzschmar, and M. Habermeyer, "Classification of full polarimetric SAR-data using artificial neural networks and fuzzy algorithms," in *Proc. IEEE Int. Geosci. Remote Sens. Symp.*, vol. 4, Jul. 1999, pp. 1995–1997.
- [21] R. Min and X. Yang, "Application of AdaBoost in polarimetric SAR image classification," in *Proc. IEEE Radar Conf.*, May 2009, no. 60772143, pp. 1–4.
- [22] G. Gigli, R. Sabry, and G. Lampropoulos, "Classifier combination and feature selection methods for polarimetric SAR classification," *Proc. SPIE, Multisensor, Multisource Inf. Fusion, Archit., Algorithms, Appl.*, vol. 6571, p. 65710B, Apr. 2007.

- [23] A. Lonnqvist, Y. Rauste, M. Molinier, and T. Hame, "Polarimetric SAR data in land cover mapping in boreal zone," *IEEE Trans. Geosci. Remote Sens.*, vol. 48, no. 10, pp. 3652–3662, Oct. 2010.
- [24] W. Yang, D. Dai, J. Wu, and C. He, "Weakly supervised polarimetric SAR image classification with multi-modal Markov aspect model," in *Proc. TC 7th Symp. 100 Years ISPRS*, vol. 38. Vienna, Austria, Jul. 2010, pp. 5–9.
- [25] V. Alberga, G. Satalino, and D. K. Staykova, "Comparison of polarimetric SAR observables in terms of classification performance," *Int. J. Remote Sens.*, vol. 29, no. 14, pp. 4129–4150, Jul. 2008.
- [26] M. Shimoni, D. Borghys, R. Heremans, C. Perneel, and M. Achteroy, "Fusion of PoLSAR and PoInSAR data for land cover classification," *Int. J. Appl. Earth Observat. Geoinf.*, vol. 11, no. 3, pp. 169–180, Jun. 2009.
- [27] L. Chen, W. Yang, Y. Liu, and H. Sun, "Feature evaluation and selection for polarimetric SAR image classification," in *Proc. IEEE 10th Int. Conf. Signal Process.*, Oct. 2010, pp. 2202–2205.
- [28] T. Zou, W. Yang, D. Dai, and H. Sun, "Polarimetric SAR image classification using multifeatures combination and extremely randomized clustering forests," *EURASIP J. Adv. Signal Process.*, vol. 2010, p. 465612, doi:10.1155/2010/465612.
- [29] Z. Qi, A. Yeh, X. Li, and Z. Lin, "Land use and land cover classification using RADARSAT-2 polarimetric SAR image," in *Proc. Tech. Commission 7th Symp., 100 Years ISPRS Adv. Remote Sens. Sci.*, vol. 38. Jul. 2010, pp. 198–203.
- [30] M. Dabboor and V. Karathanassi, "A knowledge-based classification method for polarimetric SAR data," *Proc. SPIE, SAR Image Anal., Model., Tech. VII*, vol. 5980, p. 59800C, Oct. 2005.
- [31] X. Su, C. He, Q. Feng, X. Deng, and H. Sun, "A supervised classification method based on conditional random fields with multiscale region connection calculus model for SAR image," *IEEE Geosci. Remote Sens. Lett.*, vol. 8, no. 3, pp. 497–501, May 2011.
- [32] K. Shanmugam, V. Narayanan, V. Frost, J. Stiles, and J. Holtzman, "Textural features for radar image analysis," *IEEE Trans. Geosci. Remote Sens.*, vol. GE-19, no. 3, pp. 153–156, Jul. 1981.
- [33] R. Haralick, K. Shanmugam, and I. Dinstein, "Textural features for image classification," *IEEE Trans. Syst., Man Cybern.*, vol. 3, no. 6, pp. 610–621, Nov. 1973.
- [34] F. T. Ulaby, F. Kouyate, B. Brisco, and T. H. L. Williams, "Textural information in SAR images," *IEEE Trans. Geosci. Remote Sens.*, vol. GE-24, no. 2, pp. 235–245, Mar. 1986.
- [35] F. Dell'Acqua, "Texture-based characterization of urban environments on satellite SAR images," *IEEE Trans. Geosci. Remote Sens.*, vol. 41, no. 1, pp. 153–159, Jan. 2003.
- [36] K. Ersahin, B. Scheuchl, and I. Cumming, "Incorporating texture information into polarimetric radar classification using neural networks," in *Proc. IEEE Int. Geosci. Remote Sens. Symp.*, Sep. 2004, pp. 560–563.
- [37] U. Kandaswamy, D. A. Adjeroh, and M. Lee, "Efficient texture analysis of SAR imagery," *IEEE Trans. Geosci. Remote Sens.*, vol. 43, no. 9, pp. 2075–2083, Sep. 2005.
- [38] Z. Qi, A. Yeh, X. Li, and Z. Lin, "A novel algorithm for land use and land cover classification using RADARSAT-2 polarimetric SAR data," *Remote Sens. Environ.*, vol. 118, pp. 21–39, Mar. 2012.
- [39] A. S. Solberg and A. K. Jain, "Texture fusion and feature selection applied to SAR imagery," *IEEE Trans. Geosci. Remote Sens.*, vol. 35, no. 2, pp. 475–479, Mar. 1997.
- [40] W. Yang, T. Zou, D. Dai, and Y. Shuai, "Supervised land-cover classification of TerraSAR-X imagery over urban areas using extremely randomized clustering forests," in *Proc. Joint Urban Remote Sens. Event*, May 2009, pp. 1–6.
- [41] Y. Zhang and L. Wu, "A new classifier for polarimetric SAR images," *Progr. Electromagn. Res.*, vol. 94, pp. 83–104, May 2009.
- [42] R. Dekker, "Texture analysis and classification of ERS SAR images for map updating of urban areas in The Netherlands," *IEEE Trans. Geosci. Remote Sens.*, vol. 41, no. 9, pp. 1950–1958, Sep. 2003.
- [43] D. Dai, W. Yang, and H. Sun, "Multilevel local pattern histogram for SAR image classification," *IEEE Geosci. Remote Sens. Lett.*, vol. 8, no. 2, pp. 225–229, Mar. 2011.
- [44] M. Simard, S. S. Saatchi, and G. De Grandi, "The use of decision tree and multiscale texture for classification of JERS-1 SAR data over tropical forest," *IEEE Trans. Geosci. Remote Sens.*, vol. 38, no. 5, pp. 2310–2321, Sep. 2000.
- [45] K. U. Khan and J. Yang, "Polarimetric synthetic aperture radar image classification by a hybrid method," *Tsinghua Sci. Technol.*, vol. 12, no. 1, pp. 97–104, 2007.
- [46] L. Zhang, B. Zou, J. Zhang, and Y. Zhang, "Classification of polarimetric SAR image based on support vector machine using multiple-component scattering model and texture features," *EURASIP J. Adv. Signal Process.*, vol. 2010, p. 960831, doi:10.1155/2010/960831.
- [47] A. Kourgli, M. Quarzeddine, and Y. Oukil, "Land cover identification using polarimetric SAR images," in *Proc. TC 7th Symp., 100 Years ISPRS*, vol. 38. 2010, pp. 106–111.
- [48] M. Duquenoy, J. Ovarlez, L. Ferro-Famil, and E. Pottier, "Supervised classification of scatterers on SAR imaging based on incoherent polarimetric time-frequency signatures," in *Proc. 17th Eur. Signal Process. Conf.*, 2009, pp. 764–768.
- [49] H. Yin, Y. Cao, and H. Sun, "Combining pyramid representation and AdaBoost for urban scene classification using high-resolution synthetic aperture radar images," *IET Radar, Sonar Navigat.*, vol. 5, no. 1, pp. 58–64, Jan. 2011.
- [50] D. Lu and Q. Weng, "A survey of image classification methods and techniques for improving classification performance," *Int. J. Remote Sens.*, vol. 28, no. 5, pp. 823–870, Jan. 2007.
- [51] Q. Deng, Y. Chen, W. Zhang, and J. Yang, "Colorization for polarimetric SAR image based on scattering mechanisms," in *Proc. Congr. Image Signal Process.*, May 2008, pp. 697–701.
- [52] X. Zhou and C. Zhang, "A perceptive uniform pseudo-color coding method of SAR images," in *Proc. Int. Conf. Radar*, 2006, pp. 1–4.
- [53] P. Wang, W. Hong, and F. Cao, "Investigation of the scattering intensity parameters and the hue-saturation based color space models used in the Cloude-Pottier decomposition method," in *Proc. IET Int. Radar Conf.*, Apr. 2009, pp. 1–4.
- [54] D. Turner and I. H. Woodhouse, "An icon-based synoptic visualization of fully polarimetric radar data," *Remote Sens.*, vol. 4, no. 3, pp. 648–660, 2012.
- [55] B. S. Manjunath, J. R. Ohm, V. V. Vasudevan, and A. Yamada, "Color and texture descriptors," *IEEE Trans. Circuits Syst. Video Technol.*, vol. 11, no. 6, pp. 703–715, Jun. 2001.
- [56] M. S. Lew, N. Sebe, C. Djeraba, and R. Jain, "Content-based multimedia information retrieval: State of the art and challenges," *ACM Trans. Multimedia Comput., Commun., Appl.*, vol. 2, no. 1, pp. 1–19, Feb. 2006.
- [57] T. Gevers, A. Gijsenij, J. Weijer, and J. Geusebroek, *Color in Computer Vision: Fundamentals and Applications*. New York, NY, USA: Wiley, 2012.
- [58] J. J. van Zyl, "Application of Cloude's target decomposition theorem to polarimetric imaging radar data," *Proc. SPIE, Radar Polarimetry*, vol. 1748, p. 184, Feb. 1993.
- [59] E. Krogager, "A new decomposition of the radar target scattering matrix," *Electron. Lett.*, vol. 26, no. 18, pp. 1525–1526, Aug. 1990.
- [60] J. R. Huynen, "Phenomenological theory of radar targets," Ph.D. dissertation, Faculty Electr. Eng., Math. Comput. Sci., Tech. Univ. Delft, The Netherlands, 1970.
- [61] R. Touzi, "Target scattering decomposition in terms of roll invariant target parameters," *IEEE Trans. Geosci. Remote Sens.*, vol. 45, no. 1, pp. 73–84, Jan. 2007.
- [62] Y. Kim and J. J. van Zyl, "Comparison of forest parameter estimation techniques using SAR data," in *Proc. IEEE Int. Geosci. Remote Sens. Symp.*, Jul. 2001, pp. 1395–1397.
- [63] M. Arii, J. J. van Zyl, and Y. Kim, "A general characterization for polarimetric scattering from vegetation canopies," *IEEE Trans. Geosci. Remote Sens.*, vol. 48, no. 9, pp. 3349–3357, Sep. 2010.
- [64] A. Freeman and S. L. Durden, "A three-component scattering model for polarimetric SAR data," *IEEE Trans. Geosci. Remote Sens.*, vol. 36, no. 3, pp. 963–973, May 1998.
- [65] Y. Yamaguchi, T. Moriyama, M. Ishido, and H. Yamada, "Four-component scattering model for polarimetric SAR image decomposition," *IEEE Trans. Geosci. Remote Sens.*, vol. 43, no. 8, pp. 1699–1706, Aug. 2005.
- [66] Y. Yamaguchi, A. Sato, W. M. Boerner, R. Sato, and H. Yamada, "Four-component scattering power decomposition with rotation of coherency matrix," *IEEE Trans. Geosci. Remote Sens.*, vol. 49, no. 6, pp. 2251–2258, Jun. 2011.
- [67] *Text of ISO/IEC Final Draft International Standard 15938-3 Information Technology Multimedia Content Description Interface - Part 3 Visual*, ISO/MPEG Standard N4358, Jul. 2001.
- [68] M. Pietikäinen, T. Ojala, and Z. Xu, "Rotation-invariant texture classification using feature distributions," *Pattern Recognit.*, vol. 33, no. 1, pp. 43–52, Jan. 2000.
- [69] B. S. Manjunath, P. Wu, S. Newsam, and H. Shin, "A texture descriptor for browsing and similarity retrieval," *J. Signal Process., Image Commun.*, vol. 16, nos. 1–2, pp. 33–43, Sep. 2000.

- [70] M. Partio, B. Cramariuc, and M. Gabbouj, "An ordinal co-occurrence matrix framework for texture retrieval," *EURASIP J. Image Video Process.*, vol. 2007, p. 017358, doi:10.1155/2007/17358.
- [71] M. Swain and D. Ballard, "Color indexing," *Int. J. Comput. Vis.*, vol. 7, no. 1, pp. 11–32, Nov. 1991.
- [72] E. Pottier, J. S. Lee, and L. Ferro-Famil. (2005, Feb.). Advanced concepts in polarimetry—part 1 (Polarimetric Target Description, Speckle Filtering and Decomposition Theorems), Parto of RTO-EN-SET-081—Radar Polarimetry and Interferometry Series (RTO-EN-SET-081 AC/323(SET-081)TP/47) [Online]. Available: <http://handle.dtic.mil/100.2/ADA437482>
- [73] C. Cortes and V. Vapnik, "Support-vector networks," *Mach. Learn.*, vol. 20, no. 3, pp. 293–297, Sep. 1995.
- [74] L. Breiman, "Random forests," *Mach. Learn.*, vol. 45, no. 1, pp. 5–32, Oct. 2001.
- [75] U. Kreßel, "Pairwise classification and support vector machines," in *Advances in Kernel Methods-Support Vector Learning*, B. Schölkopf, C. J. C. Burges, and A. J. Smola, Eds. Cambridge, MA, USA: MIT Press, 1999, pp. 255–268.
- [76] C. W. Hsu and C. J. Lin, "A simple decomposition method for support vector machines," *Mach. Learn.*, vol. 46, no. 1, pp. 291–314, Jan. 2002.
- [77] C. C. Chang and C. J. Lin, "LIBSVM: A library for support vector machines," *ACM Trans. Intell. Syst. Technol.*, vol. 2, no. 3, pp. 1–27, May 2011.
- [78] J. D. Wickham, S. V. Stehman, L. Gass, J. Dewitz, J. A. Fry, and T. G. Wade, "Accuracy assessment of NLCD 2006 land cover and impervious surface," *Remote Sens. Environ.*, vol. 130, pp. 294–304, Mar. 2013.
- [79] J. S. Lee, M. R. Grunes, and G. De Grandi, "Polarimetric SAR speckle filtering and its implication for classification," *IEEE Trans. Geosci. Remote Sens.*, vol. 37, no. 5, pp. 2363–2373, Sep. 1999.
- [80] M. Chi, R. Feng, and L. Bruzzone, "Classification of hyperspectral remote-sensing data with primal SVM for small-sized training dataset problem," *Adv. Space Res.*, vol. 41, no. 11, pp. 1793–1799, 2008.



Stefan Uhlmann (S'10) received the M.S. (tech.) degree in computing and electrical engineering from the Tampere University of Technology, Tampere, Finland, in 2007, where he is currently pursuing the Doctoral degree with the Department of Signal Processing.

He was a Visiting Researcher with Kodak European Research, Cambridge, U.K., from August 2008 to June 2009, and worked as a Research Scientist with Deep Visuals Ltd., Cambridge, from July 2009 to December 2009. His current research interests include remote sensing, image classification, global optimization techniques, pattern recognition, and machine learning.

Mr. Uhlmann is a Student Member of SP, EURASIP, SPIE, and Gesellschaft für Informatik e.V.



Serkan Kiranyaz was born in Turkey in 1972. He received the B.S. degree in 1994, and the M.S. degree in signal and video processing in 1996, both from Bilkent University, Ankara, Turkey, and the Ph.D. degree and his Docency from the Tampere University of Technology, Tampere, Finland, in 2005 and 2007, respectively.

He was a Researcher with the Nokia Research Center and later in Nokia Mobile Phones, Tampere, Finland. He is currently a Professor with Tampere University of Technology. He is the Architect and Principal Developer of the ongoing content-based multimedia indexing and retrieval framework, MUVis. His current research interests include multi-dimensional optimization, evolutionary neural networks, content-based multimedia indexing, browsing and retrieval algorithms, audio analysis and audio-based multimedia retrieval, object extraction, motion estimation, and VLBR video coding.